Princeton Plasma Physics Laboratory

PPPL- 4300

PPPL- 4300

Predictions of H-mode performance in ITER

R.V. Budny, R.Andre, G.Bateman, F.Halpern, C.E.Kessel, A.Kritz, and D.McCune

March 2008

Prepared for the U.S. Department of Energy under Contract DE-AC02-76CH03073.

Princeton Plasma Physics Laboratory
Report Disclaimers

Full Legal Disclaimer

Trademark Disclaimer

PPPL Report Availability

Princeton Plasma Physics Laboratory:

http://www.pppl.gov/techreports.cfm

Office of Scientific and Technical Information (OSTI):

http://www.osti.gov/bridge

Related Links:

U.S. Department of Energy

Office of Scientific and Technical Information

Fusion Links

Predictions of H-mode performance in ITER

R.V. Budny[1], R.Andre[1], G.Bateman[2], F.Halpern[2], C.E.Kessel[1], A.Kritz[2], and D.McCune[1]

(2008-04-28)

[1]PPPL, Princeton University, P.O. Box 451, Princeton, NJ 08543, USA
[2]Lehigh University, 16 Memorial Drive East, Lehigh PA 18015, USA
(email address of R.Budny: budny@princeton.edu)

Classification: MO (Reactor Physics and Design); Subject classification: 52.55.Fa (Tokamaks), 52.55.Fi (Transport), 52.55.-b (Heating), 52.55.Pi (Fusion products effects), 52.65.Qt (ICRH)

Abstract. Time-dependent integrated predictive modeling is carried out using the PTRANSP code to predict fusion power and parameters such as alpha particle density and pressure in ITER H-mode plasmas. Auxiliary heating by negative ion neutral beam injection and ion-cyclotron heating of He^3 minority ions are modeled, and the GLF23 transport model is used in the prediction of the evolution of plasma temperature profiles. Effects of beam steering, beam torque, plasma rotation, beam current drive, pedestal temperatures, sawtooth oscillations, magnetic diffusion, and accumulation of He ash are treated self-consistently. Variations in assumptions associated with physics uncertainties for standard base-line DT H-mode plasmas (with I_p=15 MA, $B_{\rm TF}$=5.3 T, and Greenwald fraction=0.86) lead to a range of predictions for DT fusion power $P_{\rm DT}$ and quasi-steady state fusion $Q_{\rm DT}$ ($\equiv P_{\rm DT}/P_{\rm aux}$). Typical predictions assuming $P_{\rm aux}$ = 50-53 MW yield $P_{\rm DT}$ = 250- 720 MW and $Q_{\rm DT}$ = 5 - 14. In some cases where $P_{\rm aux}$ is ramped down or shut off after initial flat-top conditions, quasi-steady $Q_{\rm DT}$ can be considerably higher, even infinite. Adverse physics assumptions such as existence of an inward pinch of the helium ash and an ash recycling coefficient approaching unity lead to very low values for $P_{\rm DT}$. Alternative scenarios with different heating and reduced performance regimes are also considered including plasmas with only H or D isotopes, DT plasmas with toroidal field reduced 10 or 20%, and discharges with reduced beam voltage. In full-performance D-only discharges, tritium burn-up is predicted to generate central tritium densities up to $10^{16}/{\rm m}^3$ and DT neutron rates up to 5×10^{16}/s, compared with the DD neutron rates of 6×10^{17}/s. Predictions with the toroidal field reduced 10 or 20% below the planned 5.3 T and keeping the same q_{98}, Greenwald fraction, and β_n indicate that the fusion yield $P_{\rm DT}$ and $Q_{\rm DT}$ will be lower by about a factor of two (scaling as $B^{3.5}$).

1. Introduction

One of the physics goals of ITER is to produce high rates of fusion power $P_{\rm DT}$ (around 400 MW) for long durations (around 500 s). This would enable studies of burning DT plasmas for extrapolation to the demonstration fusion power plant (DEMO). Another goal is to produce high ratios of $Q_{\rm DT} \equiv P_{\rm DT}/P_{\rm aux}$ which will be needed for DEMO. The definition of $P_{\rm aux}$ is the total auxiliary heating power with the standard convention of excluding the Ohmic power (which is predicted to be $\simeq$ 1 MW in ITER H-mode plasmas). Also discharges with high $Q_{\rm DT}$ are required in order to increase the ratio of alpha to total heating, making it easier to study this alpha heating.

It is important to have reliable predictions of $P_{\rm DT}$ and $Q_{\rm DT}$. Before the DT campaigns in TFTR [1] and JET [2] many predictions of $P_{\rm DT}$ were published. Examples are in References [3–6]. These predictions used the TRANSP code [7,8] and started with profiles measured in D-only plasmas. The time evolution of analogous DT plasmas were modeled self-consistently. For TFTR, the maximum value predicted in Ref. [5] (in 1992) for $P_{\rm DT}$ was 9.8 MW, and the maximum value predicted for $Q_{\rm DT}$ was 0.30. The maximum values measured (in TFTR in 1994) were $P_{\rm DT} = 10.1$ MW and $Q_{\rm DT} = 0.26$. The predictions for one set of JET DT discharges (Ref [3]) were up to $P_{\rm DT}$=12.4 MW and for another set of discharges (Ref. [4]) in the range 11 to 37 MW. The maximum $P_{\rm DT}$ and $Q_{\rm DT}$ measured in JET (in 1998) were $P_{\rm DT} = 15.6$ MW and $Q_{\rm DT} = 0.61$. For the JET predictions an alternative definition for the fusion gain was used, $Q'_{\rm DT} \equiv P_{\rm DT}/P_{\rm loss}$ with $P_{\rm loss} = P_{\rm ext} - dW/dt$, and the time-rate-of-change of the total energy dW/dt was relatively large for some of the record-setting shots. The rational for using $Q'_{\rm DT}$ was that its definition resembles that of the energy confinement time ($\tau_{\rm E} \equiv W/P_{\rm loss}$).

These predictions of DT performance in TFTR and JET were carried out by inputting as much experimental information as possible in the TRANSP code. Some other published simulations were less self-consistent and were carried out using less experimental data as input. These simulations predicted $P_{\rm DT}$ or $Q_{\rm DT}$ values that were considerably higher than the values later measured indicating that self-consistent integrated modeling is needed for accurate predictions of the plasma behavior.

An obstacle in producing truly validated and reliable predictions in ITER is that neither H nor D-only ITER plasmas will be available for many years. Nonetheless, predictions are needed for the design of heating systems, diagnostics, and plasma experiments. There have been major advances in tools useful for extrapolating to ITER conditions (and beyond). One approach uses databases of confinement in present experiments to study scaling in dimensionless or engineering parameters [9]. These scalings have been extrapolated to ITER. Another advance is the increased ability to make

predictions based on the underlying physics. Gyro-fluid and Gyro-kinetic-based predictive models such as GLF23 [10] are achieving significant success in predicting the evolution of measured plasma temperature profiles.

Previously, ITER predictions have been made with integrated modeling codes using partially validated models for transport and pedestal height [11–16]. It is found that predictions for the core temperature profiles and $P_{\rm DT}$ can depend sensitively on the height of the temperature pedestal at the edge of the plasma and on the stiffness of the core transport model. A transport model is said to be "stiff" if the transport fluxes increase rapidly with normalized temperature gradient once the normalized temperature gradient increases above a threshold value.

If the ITER pedestal temperature is 2.7 keV, as predicted by one of the empirical pedestal models calibrated with measurements [11], then simulations using GLF23, which is a very stiff transport model, predict fusion $Q_{\rm DT} = 4$, while simulations using the Multi-Mode (MMM95) transport model [11], and the Weiland model [17] which are less stiff, predict $Q_{\rm DT} \simeq 10$. Another prediction for the pedestal temperatures in ITER H-mode plasmas (given in Ref. [18] is 5.6 keV. Previous predictions of $P_{\rm DT}$ assuming this pedestal temperature and using all these models, GLF23, MMM95 or Weiland predict $Q_{\rm DT} \geq 10$. Fits indicate that $Q_{\rm DT}$ scales as $T_{\rm ped}^{1.9}$ in GLF23 and as $T_{\rm ped}^{0.6}$ in MMM95 [13].

Flow shear stabilization might have important effects in $P_{\rm DT}$ and $Q_{\rm DT}$ in ITER H-mode plasmas. Recent simulations that include flow shear stabilization of GLF23 transport predict significant increases in $P_{\rm DT}$, Ref. [19].

There are a number of factors that contribute to a range of predictions in the performance of ITER. Some result from uncertainties in the physics of burning plasmas. Examples of uncertainties are effects of Edge Localized Modes (ELMs), Neoclassical Tearing Modes (NTMs), density peaking, pedestal height, sawteeth, power threshold for the transition from L-mode to H-mode, He^4 transport and recycling; toroidal field ripple effects; plasma conditions in the neighborhood of the pedestal and scrape-off-layer, and the applicability of GLF23 to burning plasmas.

There are also uncertainties in the design of the heating systems, such as the negative ion neutral beam injection (NNBI) and control of density. Also there are uncertainties in the methods that will be used for initiating ITER plasmas. The lack of precision in the Ion Cyclotron Resonance Heating (ICRH) modeling (affecting the temperature predictions) and beam deposition (such as effects of ionization of excited states of beam neutrals) also contribute to uncertainty in ITER predictions.

In order to study the sensitivity of the performance of ITER to some of these uncertainties, ranges of assumptions and conditions are explored in this paper.

New ITER simulations are presented in this paper. These are carried out using the PTRANSP code, which is the TRANSP code upgraded to have more rigorous predictive capability (and renamed PTRANSP, which stands for "predictive TRANSP"). Thus PTRANSP is an extended version of a code that has had extensive and ongoing validation and verification. TRANSP is being used for the analysis of thousands of plasma shots per year from a wide variety of tokamaks, so there have been many comparisons with experiments and results have been compared with other analysis and predictive codes.

In this paper, the GLF23 transport model is used in PTRANSP for time-dependent, integrated predictions of ITER. The technique for solving stiff transport equations has recently been improved (Ref. [20]), and simulation results have been compared with experimental data from JET (Ref. [21]). Time-dependent simulations are used in order to demonstrate that burning plasmas can be created, maintained (controlled), and terminated successfully. Also time-dependent simulations are used to model phenomena such as sawtooth mixing, current diffusion, and helium ash accumulation. Full-featured integrated simulations are used in order to treat self-consistently the nonlinearities and strong coupling between the plasma, heating, current drive, confinement, and control systems.

Output data from PTRANSP are being used in other codes for further studies such as Toroidal Alfvén Eigenmode (TAE) instabilities ([22]) and diagnostic design. The phase space distributions of the fast ions, for example, are predicted. These are of interest for detailed TAE predictions and sawteeth instability ([23]). Results have been submitted to the ITPA (International Tokamak Physics Activity) profile database maintained by the Core Modeling and Database Working Group and the Transport Working Group, ([24]). The intended uses of the submissions in the databases are for code benchmarking and for inputs to down-stream analysis.

In Section 2 modeling techniques using PTRANSP are discussed. Predictions are given in Section 3 for standard ITER H-mode plasmas [25] with the full planned capabilities, *i.e.,* up to 33 MW NNBI, 20 MW He^3 minority ICRH, I_p=15 MA, and B_{TF}=5.3 T. Effects of altering the aiming of the NNBI "steering" on shine-through and beam current drive are discussed. Predictions for early operation with H-only and D-only phases are discussed in Section 4. In Section 5, results are presented for the performance of DT plasmas with the toroidal field $B_{\rm TF}$ lowered by 10 or 20% in order to consider the contingency that the full planned field will not be achieved. Conclusions are presented in Section 6. Appendix A gives details of the equilibrium calculations. Appendix B

gives details of the beam deposition, torque, and current drive. Appendix C gives details of the ICRH modeling. Appendix D gives details of recycling and helium ash modeling.

2. Modeling techniques

The Tokamak Simulation Code TSC [26], [27] is used to establish ITER discharges from an early limited plasma through the fully burning flattop phase. The self-consistent plasma equilibrium and transport evolution provides time dependent plasma boundaries, plasma density profiles, impurity fractions, injected power levels, safety factor profiles, and temperature profiles. Typically the electron density n_e profile is assumed and the GLF23 the transport [10] module is used to predict and evolve the temperature profiles.

TSC outputs are input to PTRANSP for more detailed analysis. The PTRANSP simulations of the heating, current drive, and rotation profiles can then be input back into TSC for iteration. Alternatively, PTRANSP can be run self-consistently using only the shaped boundary evolution from TSC, and computing the plasma conditions. For the results presented here this alternate method is used without iterating between TSC and PTRANSP.

For the results presented here, GLF23 [10] and NCLASS neoclassical transport [28] modules in PTRANSP are used so that the predictions of the temperature, momentum and q profiles are self-consistent across the various plasma scans. The GLF23 model is used with the default settings corresponding to the test cases provided with the GLF23 module in the NTCC Module Library Ref. [29]. Eight roots are computed and both alpha stabilization and flow shearing (with strength 1.0) are turned on. The options used for momentum transport are described in more detail below.

Computing accurate solutions for the time-evolving plasma equilibria using the Grad-Shafranov equation is very challenging. The up/down asymmetric equilibria were calculated in PTRANSP using either the ESC code [30], or TEQ [31]. Details are given in Appendix A.

The auxiliary heating powers for the standard full-performance ITER plasmas are assumed to be 16.5 or 33 MW of D-NNBI (using one or two beam lines of negative ion neutral beam injection, NNBI at 1 MeV), and up to 40 MW of ICRH near 53 MHz (tuned to the He^3 minority resonance near the plasma center).

The current ITER design allows the NNBI sources to be rotated in the vertical plane, causing the footprint of the beam in the plasma to vary over a range of approximately 50 cm vertically from discharge to discharge. It is shown in this paper that varying the NNBI aiming will

provide considerable control over plasma conditions. PTRANSP uses Monte Carlo techniques (NUBEAM, [32]) to model alpha heating and neutral beam heating, fueling, torque, and current drive. Details are given in Appendix B.

The TORIC full-wave code [33] is used to model minority ICRH. Version 5 (TORIC5) is used for the results presented in this paper. The TORIC code has been benchmarked with the AORSA code [34]. In this paper, a small fraction for the minority species density is assumed, typically $n_{\mathrm{He}^3}/n_e = 0.001$. Details of the TORIC results are given in Appendix C.

Lower Hybrid current drive can be predicted in PTRANSP using the LSC code [35], and electron cyclotron heating and current drive can be predicted by the TORAY code [36]. Both codes have been used for PTRANSP ITER H-mode predictions.

It is important to estimate the plasma rotation in ITER for several reasons: 1) It is possible to avoid deleterious resistive wall modes if the rotation speed near the plasma edge is sufficiently rapid; 2) turbulent transport might be reduced if the flow shear is sufficiently large. The toroidal velocity contributes to the radial electric field, E_r, which is calculated from force balance. Radial gradients in E_r result in flow shear, which, if sufficiently large, can in theory reduce turbulent transport. The toroidal velocity generated by the NNBI torque in ITER can be estimated by momentum balance assuming, for instance, that momentum transport is computed using the GFL23 model recently installed in PTRANSP or by taking the momentum diffusivity, χ_ϕ, simply as a fixed fraction of the ion thermal diffusivity, χ_i.

There are several methods in PTRANSP for modeling particle transport. Currently all the methods require an assumed electron density profile. As is standard for ITER modeling, n_e is assumed to be relatively flat for most of the predictions here, but peaked n_e profiles are also discussed in Subsection 3.6.

ITER plasmas are expected to contain beryllium, carbon, and tungsten impurities recycled from the walls and divertor targets, as well as argon from gas puffing in order to increase the power radiated in the divertor scrape-off flow region. Although an arbitrary number of impurities can be modeled with PTRANSP, the anticipated C and W impurities are not modeled here. The standard modeling assumptions about impurities in ITER is that they are beryllium and argon with relative concentrations $n_{\mathrm{Be}}/n_e = 0.02$, and $n_{\mathrm{Ar}}/n_e = 0.0012$, as well as thermal alpha ash and ICRH minority if applicable. Here the helium minority density is assumed to be $n_{He^3}/n_e = 0.001$. The ash transport is modeled by local conservation using the fast alpha thermalization profiles and

the wall recycling rate as sources, along with explicit transport coefficients. Details are given in Appendix D.

The fast alpha and beam ion densities are computed from the NUBRAM package. The sum of hydrogenic densities is specified by this calculation and the above assumptions and local charge neutrality, but additional assumptions are needed to determine the relative $n_{\rm D}$ and $n_{\rm T}$ profiles. These are fixed by choosing one of several models in PTRANSP. The model used here specifies a normalizing diffusivity and relative diffusivities and pinch velocities for the hydrogenic species. These were assumed to be 1 m^2 / s and unity, respectively. This model has been used successively for simulating DT emission profiles and 2D contours and trace tritium profiles in TFTR and JET [37, 38]. The model predictions for ITER are $n_{\rm D} \simeq n_{\rm T}$.

ITER H-mode plasmas are expected to have sawtooth oscillations, but the period and degree of mixing of current, plasma, and fast ions are uncertain. Large sawtooth oscillations can significantly affect the temperature and the fast ion density profiles. Sufficiently large sawtooth oscillations can trigger deleterious neoclassical tearing modes [39]. The axisymmetric effects of sawtooth oscillations were modeled in PTRANSP using a modification of the Kadomstev model [40] given a prescribed period. Also preliminary results using the Porcelli sawtooth model [41], recently installed in PTRANSP are presented.

One of the uncertainties mentioned in Sect. 1 concerns the height of the pedestal temperatures. Boundary values for the temperatures are needed for the GLF23 predictions. These can either be set as inputs in PTRANSP or computed in PTRANSP using a pedestal model [11, 42] (the NTCC PEDESTAL module). Both options have been used for the results presented in this paper. The PEDESTAL module predicts a temperature at the top of the pedestal of approximately 2.7 keV. Another prediction (for Type I ELMs given in Ref. [18]) is 5.6 keV. Since there is uncertainty regarding the height of the pedestal temperature in burning plasmas, alternative values for the pedestal temperature are assumed and their predictions are compared, as described below.

3. Predictions for the standard H-mode

The H-mode plasma regime is considered to be a likely regime for achieving a value for $Q_{\rm DT}$ around 10 [25]. Standard values are assumed for $B_{\rm TF}$ (5.3 T on axis), steady state plasma current I_p (15 MA), and plasma shaping (elongation κ_{98}=1.75, upper triangularity δ_U=0.6, and lower triangularity δ_L=0.5 at the 98 per cent flux surface). The resulting normalized pressure, β_n is in the range 1.7-1.8 which is thought to be safely below values where NTM's that might degrade confinement would occur. The value of β_n depends sensitively on the assumed electron density

profile and on the assumed values of the pedestal temperatures. The steady state phases of these plasmas are close to the conditions in the "Scenario 2" plasmas targeted for ITER. Whereas Scenario 2 specifies 40 MW of auxiliary heating out of 73 MW installed, a range of $P_{\rm aux}$ is considered here.

Various waveforms of the timing of the NNBI and ICRH are assumed. One example is shown in Fig. 1-a. One of the issues for startup is how to ramp up the heating, density, and plasma current. There are conflicting demands for the relative timing of the ramp up of density and heating. Delayed heating would reduce the shine through, but early heating might have an advantage of a lower L to H-mode power threshold.

A pressing issue for ITER is predicting the power threshold for the L to H transition. Fits to a database of present experiments in deuterium plasmas [43, 44] indicate that the threshold power in deuterium plasma would be $P_{\rm LH} \simeq 52$ MW at n_e around $0.5{\times}10^{20}/{\rm m}^3$, increasing to about 86 MW at full n_e around $1.0{\times}10^{20}/{\rm m}^3$. Experiments in JET indicate that the power threshold $P_{\rm LH}$ scales with isotopic mass as $\propto 2/A$ ([45]). This would be helpful for DT plasmas but discouraging for H-only plasmas.

In Fig. 1-a, the beam power is assumed to be ramped up in two steps. This could be achieved by either modulating each of the beam lines early or by delaying the startup of the 2nd beam line after the 1st. The first option would reduce the peak local shine through power since the beam lines view different regions of the vessel armor. The ICRH is assumed to rise briefly to 20 MW and is then decreased to 12 MW. It is assumed that the peak power will achieve H-mode confinement, and that the power can then be reduced to keep the steady state stored energy approximately constant (340 MJ). The duration of ICRH is limited in order to compare the temperature predictions and $P_{\rm DT}$ with and without ICRH. The steady state α power production is approximately 80 MW in this simulation (of which 60 MW is electron heating and 20 MW is ion heating).

The I_p ramp-up to $\simeq 15$ MA is shown in Fig. 1-b. Small oscillations in the total and Ohmic currents result from the feedback control of the free plasma boundary in TSC. Further adjustment of the gains used in TSC could reduce these, but they have negligible consequences for the predictions here. The beam-driven and bootstrap currents are also shown.

Several broad n_e profiles with a slow ramp-up to steady state were assumed. An example of a flat density profile with an abrupt roll-off into the pedestal region is shown in Fig. 2. Alternative assumptions of n_e profiles with a more gradual roll-off past x=0.9, and ones with relatively peaked

n_e were also considered, and are discussed later (in Sect. 3.6). The maximum (steady state) Greenwald fraction $f_{GW} \equiv \bar{n}_e/\bar{n}_{\rm GW}$, where $\bar{n}_{\rm Greenwald} \equiv I_p/(\pi a^2) \times 10^{20}/{\rm m}^3$, is assumed to be limited to 0.86 for standard H-mode plasmas to avoid the degradation of confinement beyond this value often seen in present experiments. The ash profile is computed using the transport model in Eq. 1 in Appendix D with the assumptions for this case that $D_{\rm ash} = 1$ m^2/s and $v_{\rm pinch} = -1$ m/s (independent of radius), and the ash recycling coefficient R is assumed to be 0.8.

The computed core $n_{\rm D}$, $n_{\rm T}$, $n_{\rm beam}$, n_α, and $n_{\rm ash}$ are perturbed by the assumed sawtooth mixing at sawtooth breaks every 50 s in this simulation. Effects of sawtooth mixing are seen in n_D, n_T, $n_{\rm beam}$, and n_α but not n_e since the n_e is assumed to not be mixed. Details of sawteeth modeling are discussed in more detail in Subsection 3.2.

The temperature profiles are predicted using the GLF23 transport model together with the NCLASS neoclassical transport model in PTRANSP. Examples of the time evolution of T_e and T_i on axis are shown in Fig. 3-a. The profiles depend sensitively on the assumed boundary values at the top of the pedestal. For the predicted temperatures shown in Fig. 3-b the pedestal temperatures are set equal to 4.9 keV (near the predictions in Ref. [18]) at the flux surface $x \equiv$ square-root of the normalized toroidal flux (approximately r/a) = 0.85.

The computed DT neutron emission rates and corresponding fusion powers are shown in Fig. 4. The beam-target emission is relatively small and there is no direct beam-beam DT emission. The $Q_{\rm DT}$ is 8.1 during the phase of highest $P_{\rm DT}$, then increases to 9.0, then 11.8 after $P_{\rm aux}$ is decreased. In other simulations with $P_{\rm aux}$ decreased to zero before termination, $P_{\rm DT}$ remains nearly constant (for many energy confinement times), implying that $Q_{\rm DT}$ becomes infinite by definition. A caveat concerning predictions of $P_{\rm DT}$ after reducing $P_{\rm aux}$ is that the response of the boundary (pedestal) temperatures is not known.

The profile of the thermal energy confinement time $\tau_{\rm E-th}$ is computed in PTRANSP as the ratio of the thermal energy and the energy loss. The latter is the flow of energy by conduction, convection, radiation, and net charge-exchange. The predicted radiated power is $\simeq 30$ MW and the net charge-exchange power loss is 0.5 MW. There is considerable uncertainty about these predictions due, in part, to uncertainties in $Z_{\rm eff}$ and the neutral density near the edge. Assumptions for the latter are discussed in Appendix D. In steady state the profile of $\tau_{\rm E-th}$, defined as the ratio of the thermal plasma energy within radius x divided by the flow of energy by conduction, convection, radiation, and net charge-exchange through x, increases slightly with x to $\tau_{\rm E-th} = 2.3$ s at the top of the pedestal. Values at larger x are not well-determined due to uncertainties such as the edge fueling,

charge-exchange, etc. The thermal ion energy confinement is larger than the electron energy confinement in these simulations.

The profile of the total energy confinement time $\tau_{\mathrm{E-tot}}$, defined similarly to $\tau_{\mathrm{E-th}}$ but using the total stored energy, is higher than $\tau_{\mathrm{E-th}}$. At the pedestal $\tau_{\mathrm{E-tot}}$ is higher by 10 %. Profiles of the angular momentum confinement are also calculated. These depend on the NNBI aiming and the assumptions used for predicting the momentum transport, discussed below. Profiles of species confinement are also computed. These depend sensitively on the assumptions of fueling and recycling.

3.1. NNBI steering

A study is carried out to investigate the effects of shifting the NNBI footprint up or down. Current plans include the ability for the beam sources to be tilted in the vertical plane to sufficiently allow about a 50 cm shift in height at the minimum tangency radius of the beam deposition. Figure 5 shows strong changes in the steady-state core beam ion density and normalized pressure β_{beam} with steering. This is predicted to have a large effect of the beam ion drive of instabilities. Examples of changes in the profile of the drive term $-R\nabla(\beta_{beam})$ are shown in Fig. 6, and compared with that for the fast alpha particles. The ability to control the profile of n_{beam} and β_{beam} with NNBI steering should be useful for separating effects of beam ions while measuring alpha effects since beam ions are predicted to be more plentiful than alphas.

Non-classical phenomena other than sawteeth that could alter the beam ion orbits, such as MHD, TAE, and anomalous diffusivity, are not modeled. The beam ions are calculated to pitch-angle scatter and slow down, remaining close to the flux surfaces where they were ionized so their density profiles are similar to their ionization profiles. The predicted beam shine-through changes very slightly with the different steering angles. Results presented here use the excited-states ionization model discussed in Appendix B.

The NNBI-driven current and total current profiles are shown in Fig. 7. The total beam currents vary from 750 kA for the case of NNBI pointed far-below-axis to 910 kA for the near-axis case. The bootstrap current is 2.6 MA, calculated using the NCLASS neoclassical code in PTRANSP. The effects of beam orientation on the q profiles at one time are shown in Fig. 8. In contrast, the effects of below-axis aiming into ITER Hybrid scenario plasmas (with $I_p = 12$ MA and higher β_n) are predicted to maintain $q(0)$ above unity for long durations ($\simeq$500 s) [46].

3.2. Sawtooth effects

As noted in the introduction, sawtooth oscillations are expected to have a significant effects on the q profile, core temperatures and on the fast ion densities. In addition, sawtooth crashes can trigger deleterious neoclassical tearing modes [39]. It is important to include sawtooth effects in the predictive modeling since, without sawtooth mixing of current, the predicted central q drops to unrealistically low values, which affects the GLF23 predicted temperatures near the magnetic axis. Unrealistic temperatures predict unrealistic values for $P_{\rm DT}$. The axisymmetric effects of sawtooth oscillations are modeled in PTRANSP using a modification of the Kadomstev model. The GLF23 model predicts the re-heating of T_e and T_i such as shown in Fig. 3-a. If the sawtooth period is short, there is not sufficient time for the central temperatures to saturate. Predictions of the density profile is not yet included in PTRANSP, but it is expected that sawtooth oscillations will have relatively little effect on the flat density profiles in these simulations of ITER. Sawtooth effects on n_e are observed in some present experiments.

A Kadomstev-like mixing of the magnetic flux was assumed in the simulations that were carried out with prescribed sawtooth periods. The effects of sawtooth crashes on the total current profile are shown in Fig. 9 indicating that the sawtooth mixing radius will be quite large in ITER. Some present experimental measurements indicate partial magnetic flux mixing, which does not diminish the sawtooth mixing radius.

Recently, a new option has been added to PTRANSP to trigger sawtooth crashes using a version of the Porcelli model [41]. Preliminary results indicate that changes in the fast ion contribution are the dominant contribution to trigger sawteeth. The sawtooth period is predicted to be considerably less than 50 s. The period and amplitude of the sawtooth crashes depends on the beam heating power and steering. The comparison in Fig. 10 of near-axis and below-axis NNBI show these effects. The H-mode with below-axis NNBI has a phase 16 MW NNBI with rapid (1.3s) sawteeth followed by slow sawteeth with 33 MW NNBI. The companion H-mode with near-axis NNBI has a relatively constant sawtooth period. An examination of sawtooth destabilization [23] found similar effects of below-axis NNBI.

NNBI steering also affects the rate of change of the central q after sawtooth crashes. Examples are shown in Fig. 11, in which the sawtooth period is fixed at 50 seconds.

Another sawtooth effect is Kadomstev-like sawtooth mixing of fast ion densities. Fig. 12 shows a strong flattening of the beam and alpha densities caused by sawtooth oscillations. Note that the peak $n_{\rm beam}$ is more than twice n_α, indicating that distinguishing alphas from beam ions might

be challenging. Also, the redistribution of fast ions after the crash could significantly increase the ripple loss of fast ions and potentially excite TAE instabilities [22].

3.3. Rotation predictions

Predictions of the NNBI-induced torque and plasma toroidal rotation profiles are shown in Fig. 13. For these simulations, the radial transport diffusivity for angular momentum χ_ϕ was assumed to be equal to the ion energy diffusivity χ_i. The steady state thermal Mach numbers (v_{tor}/v_{sound}) of the central D and T rotation speeds is 0.05. The corresponding Mach number for the carbon impurity is 0.125. For comparison, Mach numbers of hydrogenic species with co-current neutral beam injection into TFTR, JET, and DIII-D have often achieved values near and sometimes above 0.5.

As seen in Fig. 13, the central rotation is affected by the NNBI aiming. Also the momentum confinement time τ_ϕ is affected. For the simulations shown in Fig. 13, the steady state profiles of τ_ϕ are around 1.0 s in the core and decrease with x near the pedestal. Values at x=1 are 0.8 - 1.0 s.

An example of the radial electric field from force-balance is shown in Fig. 14. The contribution from the poloidal rotation, $v_{\rm pol}$ is calculated from NCLASS neoclassical model [28]. It can be seen that the toroidal velocity contribution to the magnitude of the radial electric field dominates everywhere in the plasma except in the pedestal region. The peak value of $E_{\rm r}$ is comparable to values that have been measured routinely in TFTR, JET, and DIII-D.

If the ratio χ_ϕ/χ_i is lowered, the predicted rotation rate increases. An example of a scan in χ_ϕ/χ_i from 1.0 down to 0.1 is shown in Fig. 15-a. At the lowest value assumed, $\chi_\phi/\chi_i = 0.1$, the χ_ϕ profile is near neoclassical and the profile of T_i, shown in Fig. 15-b, develops an internal transport barrier (ITB) as a result of $E \times B$ flow shear stabilization turbulence. A similar result was reported in Ref. [19] when the NNBI power and thus torque is sufficiently large. In reference [19] it was found this barrier occurred with modest levels of NNBI powers around 10 MW.

Kinsey *et al,* [47] argued that the feedback between increased confinement and increased flow shear stabilization may be the cause of ITB formation in DIII-D. If this will occur in ITER it should lead to increased performance so this possibility merits further investigation.

3.4. Recycling

There is uncertainty in the helium ash transport and recycling. One important issue is whether there is an inward pinch of the helium ash. If there is an inward pinch, the central ash density and $P_{\rm DT}$ will depend sensitively on the ash recycling coefficient R. If there is an outward or zero pinch, $P_{\rm DT}$ is predicted to depend weakly on R. Several scans were carried out varying assumptions about the transport and recycling. The transport assumptions are summarized in Table 1. For one scan, an inward pinch was assumed, and for two others an outward pinch was assumed. Details are discussed further in Appendix D. Examples of the quasi-steady state ash densities in two of these cases are shown in Fig. 16.

For the scan assuming an inward pinch, the central ash density increases in time to steady state values depending on R. The n_e profile is assumed fixed, so that increasing R depletes the deuterium and tritium fuel. Results for the dependence of the development of helium ash and the DT fusion rate as functions of R are shown in Fig. 17. As R increases from 0.6 to 0.95, an increasing amount of helium ash accumulates in the core and the fusion power production is significantly reduced. The total number of ash ions, shown in Fig. 17-a, decreases by lower increments as R decreases. Like-wise, $P_{\rm DT}$ increases by lower increments as R deceases. The computed ratio $\tau^*_{\rm ash}$ / $\tau_{\rm E-tot}$ ranges from 3 to 22. For ITER with standard pumping, this ratio is predicted to be 2 to 4 [48].

3.5. Effects of pedestal assumptions

Various assumptions were explored for setting the pedestal temperatures. One option was to use the PEDESTAL module, which predicts a pedestal temperature equal to 2.7 keV for full current (15 MA) discharges in ITER. Since there are uncertainties associated with extrapolations to burning plasmas, simulations were carried out with the pedestal temperatures increased or decreased. Examples with 33 MW D-NNBI and 20 MW ICRH are shown in Fig. 18. The peak values of $P_{\rm DT}$ were 100, 235, and 445 MW indicating the sensitivity to the assumed pedestal temperature.

A related uncertainty results from the gap between the region where GLF23 is well-tested and believed to be applicable, (r/a less than 0.8) and the likely location of the pedestal (r/a around 0.95 or greater). The extrapolations over this range were done assuming either that GLF23 is valid to large values of r/a or that the transport is given by a multiple of the Chang-Hinton values, bounded between 100 m^2/s and 0.01 m^2/s. One difficulty in extending GLF23 into the pedestal is that the model is sensitive to the electron density gradient and large gradients cause low temperature gradients, reducing temperatures further in. If the specified χ_i is too high or too low in this region the predicted temperatures have a flat plateau or abrupt drop to maintain the

specified pedestal value. Although the predicted core temperatures and $P_{\rm DT}$ are effected, they typically do not vary strongly with these assumptions regarding transport in this gap region.

3.6. Peaked density

The simulations presented so far assumed that the electron density profile n_e is flat with an abrupt drop near the pedestal, as shown in Fig. 2-b. Simulations were also carried out assuming a flat n_e with a less precipitous drop near the pedestal, and the results are similar to those presented above. In addition simulations were also carried out with the mildly peaked n_e shown in Fig. 19-a. The rational for considering such peaked profiles is that some experiments indicate that plasma density profiles tend to become more peaked as the normalized collisionality ν_* becomes lower approaching values expected in ITER [49].

The PTRANSP simulations with the GLF23-predicted temperatures indicate that and fusion power tend to be low with such a peaked n_e profile. This result is due to transport becoming larger (in GLF23) as the density-gradient-driven trapped particle modes dominate. The $P_{\rm DT}$ is 140 MW. Neutron emission from two simulations with differing assumptions of sawtooth mixing, and beam aiming are shown in Fig. 19-b.

A similar result for Hybrid scenario plasmas in ITER was reported in Ref. [50]. It was found that very large pedestal temperatures ($\simeq$ 10 keV) are needed to produce peaked-density Hybrid plasmas with high β_n ($\simeq 3$).

Generally the transport is expected to be reduced with moderate peaking as long as the density gradients below the threshold where the TEM becomes unstable. This was not seen in the above-mentioned simulations, perhaps due to assuming a boundary for the GLF23 temperatures too far into the large density gradient region ($r/a = 0.9$). The predicted χ_i and χ_e were large past $r/a = 0.75$.

3.7. Alternatives to the standard regime

Variations around the standard DT H-mode (with 33 MW NNBI and Greenwald fraction around 0.86) were considered. Examples include using only one beam line with 17.5 MW, adding 40 MW ICRH instead of the usual 20 MW, and adding LHCD or ECH/ECCD. For instance 30 MW of LHCD is predicted to drive up to 0.9 MA. The peak in the driven current moves, as the plasma ramps up, in from x from 0.9 to 0.75 (x is the square-root of the normalized toroidal flux) causing a slight perturbation of the q profile around $x = 0.8$ to 0.9.

Predictions were done with Greenwald fraction increased to 0.94 and $P_{\rm aux} = 50$ MW corresponding to the more aggressive "Scenario 1". Predictions with optimistic assumptions ($T_{\rm ped}$ around 6keV and outward ash pinch) achieved $P_{\rm DT}$ and $Q_{\rm DT}$ greater than 750 MW and 20.

Because of the stiffness of the transport model, additional heating power tends to produce only slightly higher temperatures and fusion yield, but sometimes lower $Q_{\rm DT}$. The scaling of $Q_{\rm DT}$ is predicted to be $P_{\rm aux}^{-0.9}$ with GLF23 and $P_{\rm aux}^{-0.5}$ with MMM95 [13]. That is, the fusion power does not increase as rapidly as the input heating power. The main benefit of higher $P_{\rm aux}$ appears be increased insurance of accessing the H-mode regime and controlling the plasmas.

4. H-only and D-only plasmas for early operation

A long phase of testing and experiments with H plasmas in ITER is planned. A phase of D-only plasmas before the DT phase is not planned since the production of T from D+D $\rightarrow$ T+n is expected to cause enough DT neutrons to require full nuclear licensing.

Due to concern about excessive shine-through, the NNBI in the H-only phase is expected to be limited to 8-10 MW (from one beam-line) at 500-870 keV. The ICRH heating during the H-phase has not been determined, but He^3 or He^4 minority is being considered, along with D fundamental heating at reduced $B_{\rm TF}$. The lower $P_{\rm NNBI}$ and lack of fusion heating reduces the temperatures predicted by GLF23 unless the pedestal temperature is sufficiently high. The pedestal model built into PTRANSP [42] becomes activated when the power flow into the pedestal region is sufficient to trigger an L-mode to H-mode transition according to the Snipes scaling [51, 52]. Since this condition is not met with low input power, the simulation defaults to applying input pedestal temperatures. Examples of temperature predictions in an H-only plasma are shown in Fig. 20. Results are shown for a range of pedestal temperatures and for 20 MW or 40 MW of ICRH in addition to the 8 MW NNBI heating.

Although D-only plasmas are not planned during the early operation of ITER, simulations were carried out for D-only plasmas in order to assess the tritium and DT neutron production rates in D-only plasmas. In these simulations, it is assumed that one D-NNBI is used, delivering 17 MW D ions at 1 MeV in addition to 20 or 40 MW of ICRH. The results for the neutron emission are plotted in Fig. 21. The DT neutron rate is lower than the DD neutron rate by more than an order of magnitude.

5. Reduced performance H-mode

There is a concern that ITER may need to operate with reduced toroidal magnetic field $B_{\rm TF}$ or reduced NNBI voltage. In order to address these concerns, H-mode DT plasmas with $B_{\rm TF}$ reduced by 10% or 20% are modeled. In these simulations the plasma current, I_p, was reduced in proportion to maintain the same edge q-profile ($q_{98} \simeq 4$). To maintain the Greenwald fraction at the recommended value (0.86) and maintain the effective impurity concentration $Z_{\rm eff}$ approximately the same, the densities n_e, $n_{\rm Be}$, and $n_{\rm Ar}$ were reduced proportionately. Lastly, to keep β_n constant (near 1.7), the pedestal temperatures were reduced. Since β scales as the ratio of pressure to $B_{\rm TF}^2$, and since $B_{\rm TF}$ and n_e scale together for constant Greenwald fraction, the pedestal temperatures need to also scale as $B_{\rm TF}$. These reductions have a dramatic effect on the fusion power production $P_{\rm DT}$.

Figure 22 shows the computed electron temperatures, T_e, for four predictions, and Fig. 23 shows the corresponding ion temperatures, T_i. The central temperatures are shown as a function of time in the left panels while the temperature profiles at 245 s, just before a sawtooth crash, are shown in the right panels of these figures. The heating powers computed by these simulations are summarized in Table 3. Note that $P_{\rm DT}$ and P_α decrease rapidly with decreasing $B_{\rm TF}$. It is found that in these simulations, $P_{\rm DT}$ is found to scale as $B_{\rm TF}^{3.5}$. Note also that alpha parameters such as the average normalized pressure of the fast alpha particles, $\langle\beta_\alpha\rangle$ are reduced weakly with $B_{\rm TF}$, since they scale with the temperatures.

Figure 24 shows alternative comparisons with $B_{\rm TF}$ reduced 20%. The heating was assumed to be 33MW NNBI and 20MW ICRH with the steady state central n_e fixed at $0.84\times10^{20}/m^3$. In addition, the NNBI aiming was varied in the simulations (while holding the sawtooth period fixed at 50 s) showing a strong effect in the temperature reheat after each sawtooth crash. Another simulation assumed a higher pedestal temperature, which increased β_n from 1.7 to 2.1. An additional simulation was carried out with the plasma current I_p increased from 12 MA to the reference 15 MA, which altered the q profile. Results are summarized in Table 4.

Another variation considered for the standard H-mode is the beam voltage. Lower voltage than the nominal goal of 1 MeV has several advantages, such as reducing the shine-through and increasing the total torque for a given NNBI power. Some of the disadvantages of lower beam voltage are lower core heating and lower beam-driven current.

Three simulations were carried out to explore effects of lower NNBI voltage. The beam voltages considered were 750, 500, 250, and 120 keV. The injected power is expected to be lower with lower

voltage, but it was fixed at 33 MW for purposes of comparison. Since injection at 120 keV is not feasible with NNBI, positive ion NBI would be needed. The positive ion source would emit atomic, diatomic, and triatomic ions with full, half, and third energies. The neutralization efficiency for hydrogenic ions decreases rapidly above velocities near the Bohr velocity, corresponding to energies of about 40, 80, and 120 keV for H, D, and T. It was assumed that the 120 keV NBI used D with the current at the full energy reduced from 100% for the NNBI cases to 40%, the half-energy fraction to 20%, and the third-energy fraction to 40%. These assumed values are roughly consistent with values achieved in the TFTR, JET, and DIII-D tokamaks. Note that the energy fractions would be even much less favorable for H-NBI.

The NNBI steering was assumed to be aimed below-axis (close to the vessel midplane) for the scan. The pedestal model was used to predict the pedestal height, resulting in $T_{\rm iPed} = T_{\rm ePed} = 2.9$ keV. Radial profiles for the dominant beam ionization rate, ionization of thermal D and T ions, are shown in Fig. 25-a. The increased ionization rate decreases the shine-through. The decrease in penetration with lower beam voltage shown in Fig. 25-b is dramatic. The shine-through for 120 keV beams is negligible. The beam-driven current also shows a dramatic decrease with decreasing beam voltage, as shown in Table 5.

The predicted torque profiles are shown in Fig. 26-a. The volume-integrated profiles are shown in Fig. 26-b. Predictions for the rotation profiles are shown in Fig. 27. The rotation rate at the $q = 2$ rational surface is predicted to double as the voltage is reduced from 1 MeV to 120 keV. Since the effects of sheared rotation in the GLF23 model were not modeled, the temperature profiles are nearly constant in this scan. It is not clear whether the inclusion of flow shear effects will significantly alter the temperature predictions significantly.

6. Discussion and summary

PTRANSP simulations using the GLF23 transport model and the NCLASS neoclassical transport model are used to predict the performance of H-mode discharges in ITER. To account for various physics and technology uncertainties, scans were used to estimate the range of predictions. Simulations with 33 MW of D-NNBI at 1 MeV and 20 MW ICRH at 53 MHz, results in approximately 250 to 720 MW of fusion power production (α particles and neutrons) corresponding to $Q_{\rm DT} \approx 5$ - 14. Much lower values of $P_{\rm DT}$ are predicted with adverse assumptions of alpha ash accumulation. Much higher values (even infinite) for $Q_{\rm DT}$ are predicted in optimistic cases where $P_{\rm aux}$ is lowered before plasma termination and $P_{\rm DT}$ maintains a nearly constant value for many energy confinement times. In simulations for the baseline cases, it is assumed that the boundary electron and ion temperatures are in the range 2.5-5 keV at a boundary r/a set around 0.80-0.95.

The toroidal rotation velocity, which contributes to flow shear stabilization of turbulent transport, is computed using the assumptions that the toroidal momentum diffusivity is proportional to the ion thermal diffusivity, or using values predicted by GLF23.

It is found that the neutral beam deposition is affected strongly when steering is used to aim the NNBI up or down relative to the midplane. The sawtooth crash amplitude and period predicted by the Porcelli model is also affected by neutral beam steering. In particular, below-axis aiming decreases the sawtooth period, which can be an important tool in controlling the seed islands that trigger neoclassical tearing modes. The heating and pressure profiles can be changed by steering neutral beams and, consequently, the flow shear rate and confinement are changed. The predicted shine-through does not change appreciably with different steering angles. Simulations carried out with reduced neutral beam injection voltage demonstrate reduced shine-through and increased heating and torque near the edge of the plasma.

Various assumptions for the ash transport and recycling coefficient are explored. If there is an inward pinch, then the ash density in the core will depend sensitively on the value of the recycling coefficient, which depends on plasma conditions near the separatrix and in the scrape off region, and on the exhaust pumping capabilities. If the recycling coefficient is close to unity, then the fusion power will be low.

Simulations carried out with the toroidal magnetic field reduced by 10% or 20% demonstrate severe reductions in performance. As the toroidal magnetic field is reduced in these simulations, the plasma current is reduced to maintain the same q profile, the density is reduced to maintain the same Greenwald fraction, and the pedestal temperature is reduced to maintain the same value of β_n. It is found that the fusion power production scales approximately as $B_T^{3.5}$ under these conditions.

The range of $P_{\rm DT}$ and $Q_{\rm DT}$ found in these simulations include values low compared with the goals for ITER H-mode performance. There are many possibilities that could make the actual achievements better than the predictions given here. Examples include the possibility that more optimistic temperature models, such as the less-stiff Multi-Mode model might be more accurate for ITER, or that the product $n_{\rm D}n_{\rm T}$ can be made larger, say if good confinement can be achieved when the Greenwald fraction is higher than assumed.

The range of predictions for $Q_{\rm DT}$ includes values lower than some other published ITER predictions. This is reflected in the relatively low values predicted for $\tau_{\rm E-th}$ compared with the

extrapolations from database studies. There are several causes of these low predictions. One is that the simulations from GLF23 tend to be less optimistic than those of less stiff models such as the Multi Mode and Weiland models. The GLF23 simulations depend strongly on the assumptions of the boundary temperatures. The values assumed here (at the top of the pedestal) are motivated by two fits, the lowest (from Ref. [11, 42] is near 2.7 keV, and the other (from Ref. [18]) is 5.6 keV. Comparable low values for $Q_{\rm DT}$ have been predicted before using GLF23 with the low boundary temperatures. The relatively low values predicted here for the higher boundary temperatures are due to a combination of effects resulting from adding features such as sawtooth mixing (that lowers the average central T_i and alters the q profile) and ash accumulation. Clearly more work is needed to improve the confidence in ITER predictions.

New and unexpected regimes and physics have been discovered in each new tokamak on the forefront of fusion research. Examples include the discovery of the L-mode around 1980, the H-mode in 1982, and the development of hot ion modes starting in the 1970's. Some of these discoveries have had significant implications for practical fusion power production. The simulations presented in this paper could be considered as a baseline beyond which new discoveries could lead to improved advanced tokamak performance. Since ITER will be such a large step beyond present experience, there is a significant likelihood that new discoveries will lead to results that extend well beyond the baseline performance.

Acknowledgments

PTRANSP is being developed by a collaboration between PPPL, Lehigh University, LLNL, and GA. We wish to acknowledge the contributions of the collaborators, especially Jon Kinsey (GA) for benchmarking one of the predictions (20100G21 shown in Fig. 18 and elsewhere) using GLF23 in the XPTOR code. We also thank Lee Berry and his team at ORNL for benchmarking one of the TORIC results with the AORSA code. This work is supported in part by the US DoE Contracts No. DE-AC02-76CH03073 and E-FG02-07ER54927.

Appendix A Equilibrium solutions

Most of the results use the TEQ equilibrium code, which computes more accurate solutions for the challenging central pressure profiles. TEQ is run in a prescribed boundary mode, using input q and pressure profiles, and matches $F = RB_{\rm tor}$ at the plasma edge. In order to match the total plasma current TEQ is called iteratively with adjustment to the edge q profile. Since TEQ tends to display a sensitivity to the pressure profile around the axis, which can fluctuate due to Monte Carlo noise, the pressure profile is smoothed near the axis and, optionally, any hollowness in the pressure profile near the axis is removed. Examples of profiles for one of the simulations with below-axis NNBI is shown in Fig. 28.

An example of the error in an equilibrium solution with TEQ is shown in Fig. 29. The error, which is defined as the relative difference between the two sides of the Grad-Shafranov equation normalized by the area-average, is seen to be generally below 5 per cent. The corresponding error for the ESC equilibrium code solution is larger than this over much of the 2D plane. The free boundary equilibrium solver in TEQ is currently being integrated into PTRANSP.

Appendix B Beam modeling

PTRANSP uses Monte Carlo methods (Ref. [32]) to calculate beam deposition, beam torque, as well as the slowing down, pitch-angle scattering, and thermalization of beam ions and fusion ions. For the simulations presented here, the number of Monte Carlo particles used was 1000 for the beam ions and alpha particles.

The beam ionization rate is required for determining the beam deposition and shine through. The beam deposition is needed for calculating the profiles of the beam density, heating, current, and torque. The data for deposition of 1MeV beams is not well established. Two of the uncertainties are the impact ionization rates on impurities and the multi-step ionization of excited states of beam neutrals.

These rates have been studied in several papers, [53–57]. Reference [53] assumes that the impurity ionizations, Z_{imp} does not vary in time. In Ref. [55] impurity stopping is based on interpolation of Carbon and Oxygen cross sections. With this data the Z_{imp} may vary in time. The model in [56] gives ionization rates close to those in Ref. [55].

PTRANSP uses cross sections modified from Ref. [54] updated by Boley (private communication). The PTRANSP cross sections are very close to those in Ref. [56] around 100 kV/amu. The option

to include the excited states calculation of Ref. [55] can be used. Profiles for a representative simulation are shown in Fig. 30. The dominant rate is the thermalization on thermal hydrogenic ions.

PTRANSP comparisons with and without the multi-step ionization model show mild effects in the deposition profiles but factor-of-two differences in the shine-through power and loading on the vessel armor. Fig. 31 shows a simulation with below-midplane aiming.

Experiments with NNBI shine-through in JT-60U Ref. [58] indicate that the simple model is consistent with calorimetry measurements of heating Ref. [59].

Whether the shine-through loading shown in Fig. 31-b is tolerable depends on the footprint of the loading. Since the design of the beam system has not been finalized. the specifications of the beam geometry have not been finalized. The preliminary design Ref. [60] provides a complicated set of specifications for an optimistic, well-focused geometry and a less well-focused geometry. Beam footprints and geometries in both cases have been presented Ref. [61].

The well-focused beam parameters, shown in Table 6, are used in this paper. Examples of beam-neutral trajectories for the tight-geometry case with below-midplane steering are shown in Fig. 33. The injection was assumed to be in the co-I_p and co-$B_{\rm TF}$ directions. An ITER design document, Ref. [62] indicates that the transient (up to 10s) power load limit for the armor will be 0.5 to 1.4 MW/m^2. This limit appears to be exceeded by a factor of about four in the prediction with excited states ionization in Fig. 31-b. The predicted power loading with the same plasma startup could be reduced by a factor of four by delaying the start of NNBI until about 80s, at which time the plasma density is higher.

Since there are uncertainties in the cross sections and in the excited states ionization rates, simulations were performed to assess variations in the shine-through with the cross sections varied up or down by 20 percent. Figure 32 shows results for simulations of 10 MW H-NNBI at 870 keV into H plasma as the density is ramping up. This shows a strong sensitivity to the values of the cross section assumptions.

The NNBI torque is calculated carefully in PTRANSP. Examples of the profiles used for the total torque are shown in Fig. 34. With the NNBI torque profile, the assumption $\chi_\phi \simeq \chi_i$ results in relatively low rotation rates. The values of the poloidal rotation rate $v_{\rm pol}$ predicted by the NCLASS [28] neoclassical module in PTRANSP are also relatively small.

Appendix C ICRH modeling

The TORIC5 code was used to model the ICRH. The frequency was chosen to be 52.5 MHz and the minority ion He^3. The phasing of the antenna straps was assumed to be $(0, \pi, 0, \pi)$. The number of poloidal modes was 31 and the number of mesh points was 64. The number of toroidal mesh points was 64. The number of radial mesh points was 203. PTRANSP can run TORIC with a spectrum symmetric in the toroidal wave number n_ϕ. For the runs used here the spectrum was assumed to have two peaks at one value of $|n_\phi|$. Two choices were used: 27 and 41. For the standard DT H-mode plasmas the corresponding parallel indices were $n_{||}(0) = 3.85$ and 5.88, and the equivalent wave numbers $k_{||}$ were 4.24 and 6.47 m^{-1}.

Examples of contours of $Re(E_+)$ are shown in Fig. 35. The contour plots indicate that the TORIC5 runs are well converged. Another check showing convergence is that the computed absorbed and radiated $J * E$ and Poynting powers are approximately equal. Results show a relatively large fraction of the ICRH heating is on electrons and thermal ions. Profiles are shown in Fig. 36 and total powers are listed in Table 7.

Appendix D Recycling and helium ash transport

PTRANSP has many modes for modeling the transport of the hydrogenic and impurity ions. The modeling reported here specified relative transport of the hydrogenic ions. The n_D and n_T profiles are not very sensitive to this specification The thermalized He ash profile evolves in time in PTRANSP simulations, and the computed profiles are very similar. The rates for gas fueling and recycling sources for each of these were assumed to be 1×10^{21} s^{-1}. For comparison, the minimum needed to replenish the tritium burnup is about 1.5×10^{20} s^{-1} and the total deuterium fueling rate from 33 MW of D-NNBI at 1 MeV is 2×10^{20} s^{-1}. Higher gas and wall fueling rates would lead to lower particle confinement and larger density of neutrals in the plasma edge and, thus, higher rates of charge-exchange losses. The values of the D and T confinement times around $x = 0.95$ are about 100 s. The values of the total charge-exchange power loss is about 0.5 MW in standard DT plasmas.

The accumulation of He ash is simulated in PTRANSP assuming a form for the transport such as:

$$\Gamma_\mathrm{ash} = (-D_\mathrm{ash} \nabla n_\mathrm{ash} + V_\mathrm{ash} n_\mathrm{ash}) A_\mathrm{surf}, \tag{1}$$

where A_surf is the flux surface area and D_ash and V_ash are the flux surface averaged diffusion and convection velocity. The ash density, n_ash, is calculated from the local source of thermalizing fusion alphas and recycling influx from the wall. The recycling coefficient of the ash, R, defined as the ratio of the fluxes entering and exiting the plasma boundary, $\Gamma_\mathrm{in}/\Gamma_\mathrm{out}$, needs to be assumed as

well. At fixed electron density, the fusion rate decreases to low values as R is increased towards unity.

Thermalized alpha ash can have significant effects, especially if there is an inward pinch. The ash accumulation was simulated using various choices of the radial transport (Eq. 1) and the ash recycling coefficient R. Two cases of transport with an inward pinch and one with an outward pinch were investigated. They are summarized in Table 1. Examples are shown in Fig. 16-17. In the cases with an assumed large inward pinch, the transport causes a peaking of $n_{\rm ash}$ and a slight peaking of $Z_{\rm eff}$. The central $Z_{\rm eff}$ increases from 1.74 to 1.97 as the recycling coefficient R is increased from 0.6 to 0.9. The fusion power drops from 235 to 160 MW

Values of the effective ash recycling coefficient, $\tau^*_{\rm ash} \equiv N_{\rm ash}$ / $\Gamma_{\rm ash}$ / $(1-R)$, which vary from 3 to 20 times the energy confinement time $\tau_{\rm E-tot}$, are shown in Table 2. Typically ITER predictions assume that $\tau^*_{\rm ash}$ / $\tau_{\rm E-tot}$ is less than 5 or 10.

The values for the D and V profiles were arbitrarily chosen for the inward pinch case to be $1{\rm m}^2/s$ and $-1{\rm m}/s$, and for the outward pinch case to be $0.1{\rm m}^2/s$ and $+0.1{\rm m}/s$.

[1] HAWRYLUK, R., Reviews of Modern Phys. **70** (1998) 547.
[2] KEILHACKER, M., GIBSON, A., GORMEZANO, C., et al., Nucl. Fusion **39** (1999) 209.
[3] STUBBERFIELD, P., BALET, B., and CORDEY, J., Plasma Phys. Controlled Fusion **33** (1991) 1255.
[4] BALET, B., CORDEY, J. G., GIBSON, A., et al., Proc. 21st EPS Conf. on Plasma Physics (Montpellier, 1994) **18B** (ECA) 5 **18B** (1994).
[5] BUDNY, R. V., BELL, M. G., BIGLARI, H., et al., Nucl. Fusion **32** (1992) 429.
[6] BUDNY, R. V., Nucl. Fusion **34** (1994) 1247.
[7] GOLDSTON, R. J., MCCUNE, D. C., TOWNER, H. H., DAVIS, S. L., and *ET AL.*, J. Comput. Phys. **43** (1981) 61.
[8] BUDNY, R. V., Nucl. Fusion **42** (2002) 1383.
[9] THOMSEN, K., CORDEY, J., KARDAUN, O., and ITPA H-mode Database WG, Proc. 31st EPS Conf. on Plasma Physics (London, UK, 2004) **28G**.
[10] WALTZ, R. E., STAEBLER, G. M., DORLAND, W., et al., Phys. Plasmas **4** (1997) 2482.
[11] BATEMAN, G., ONJUN, T., and KRITZ, A., Plasma Phys. Controlled Fusion **45** (2003) 1939.
[12] KINSEY, J. E., BATEMAN, G., ONJUN, T., et al., Nucl. Fusion **43** (2003) 1845.
[13] KINSEY, J. E., STAEBLER, G. M., and WALTZ, R. E., Fusion Science and Technol. **44** (2003) 763.
[14] PACHER, G. W., PACHER, H. D., KUKUSHKIN, A. S., JANESCHITZ, G., and PEREVERZEV, G., Nucl. Fusion **43** (2003) 188.
[15] MUKHOVATOV, V., SHIMOMURA, Y., POLEVOI, A., et al., Nucl. Fusion **43** (2003) 942.
[16] ONJUN, T., KRITZ, A., BATEMAN, G., and PARAIL, V., Phys. Plasmas **12** (2005) 082513.
[17] BATEMAN, G., KRITZ, A. H., REDD, A. J., and WIELAND, J., Plasma Phys. **5** (1998) 1798.
[18] SUGIHARA, M., MUKHOVATOV, V., POLEVOI, A., and SHIMADA, M., Plasma Phys. Controlled Fusion **45** (2003) L55.
[19] STAEBLER, G. M. and JOHN, H. E. S., Nucl. Fusion **46** (2006) L6.
[20] JARDIN, S. C., BATEMAN, G., HAMMETT, G. W., and KU, L. P., On 1D diffusion problems with a gradient-dependent diffusion coefficient, 2007, submitted to J. Comp. Phys.
[21] BATEMAN, G., KRITZ, A., HALPERN, F., et al., Bull. Am. Physical Society, Oct. 2006, JP1 126.
[22] GORELENKOV, N. N., BERK, H. L., and BUDNY, R. V., Nucl. Fusion **45** (2005) 226.
[23] CHAPMAN, I., PINCHES, S. D., BUDNY, R. V., et al., Plasma Phys. Controlled Fusion **49** (2007) B385.
[24] ROACH, C. M., WALTERS, M., BUDNY, R. V., et al., The 200x public release of the international multi-tokamak confinement profile database, to be submitted.
[25] CAMPBELL, D. J., Plasma Phys. **8** (2001) 2041.
[26] JARDIN, S. C., POMPHREY, N., and DELUCIA, J., J. Comput. Phys. **46** (1986) 481.
[27] KESSEL, C. E., GIRUZZI, G., SIPS, A. C. C., et al., Nucl. Fusion **47** (2007) 1274.
[28] HOULBERG, W. A., SHANG, K. C., HIRSHMAN, S. P., and ZARNSTORFF, M. C., Phys. Plasmas **4** (1997) 3230.
[29] KRITZ, A. H., BATEMAN, G., KINSEY, J., et al., Comput. Phys. Commun. **164** (2004) 108.
[30] ZAKHAROV, L. E. and PLETZER, A., Plasma Phys. **6** (1999) 4693.
[31] DECTYAREV, L. and DROZDOV, V., Computer Physics Reports 2 **7** (1985) 341.
[32] PANKIN, A., BATEMAN, G., BUDNY, R., et al., Comput. Phys. Commun. **164** (2004) 421.
[33] BRAMBILLA, M., Plasma Phys. Controlled Fusion **41** (1999) 1.
[34] BERRY, L. A., BATCHELOR, D. B., BONOLI, P. T., et al., Fusion Energy 2006 (Proc. 21st Int. Conf. Chengdu, 2006) (Vienna: IAEA) CD-ROM file TH/P6-8 and http://www-naweb.iaea.org/napc/physics/FBC/FEC2006/html/inded.htm .
[35] IGNAT, D. W., VALEO, E. J., and JARDIN, S. C., Nucl. Fusion **34** (1994) 837.
[36] KRITZ, A. H., HSUAN, H., GOLDFINGER, R. C., and BATCHELOR, D. B., 1982 Conf. Proc. 3rd Int.

Symp. on Heating in Toroidal Plasmas ECE (Brussels, Belgium) **2** (1982) 707.
[37] BUDNY, R. V., ERNST, D. R., HAHM, T.-S., et al., Phys. Plasmas **7** (2000) 5038.
[38] VOITSEKHOVITCH, I. and JET EFDA Contributors, Plasma Phys. **12** (2005) 052508.
[39] SAUTER, O., WESTERHOF, E., MAYORAL, M., et al., Phys. Rev. Lett. **88** (2002) 105001.
[40] KADOMTSEV, B. B., Sov. J. Plasma Phys. **1** (1975) 389.
[41] PORCELLI, F., BOUCHER, D., and ROSENBLUTH, M., Plasma Physics and Controlled Fusion **38** (1997) 2163.
[42] ONJUN, T., BATEMAN, G., KRITZ, A. H., and HAMMETT, G., Plasma Phys. Controlled Fusion **45** (2003) 1939.
[43] RYTER, F. and the H-mode Threshold Database Group, Plasma Phys. Controlled Fusion **44** (2002) A415.
[44] MARTIN, Y. and CDBM H-mode Threshold Database Working Group, submitted (2007).
[45] RIGHI, E., BARTLETT, D. V., CHRISTIANSEN, J. P., et al., Nucl. Fusion **39** (1999) 309.
[46] BUDNY, R. V., KESSEL, C. E., KINSEY, J. E., et al., Fusion Energy 2006 (Proc. 21st Int. Conf. Chengdu, 2006) (Vienna: IAEA) CD-ROM file IT/P1-5 and http://www-naweb.iaea.org/napc/physics/FBC/FEC2006/html/inded.htm .
[47] KINSEY, J. E., STAEBLER, G. M., BURRELL, K. H., AUSTIN, M. E., and WALTZ, R., Phys. Rev. Lett. **86** (2001) 814.
[48] KUKUSHKIN, A. S., PACHER, H. D., PACHER, G. W., et al., Nucl. Fusion **43** (2003) 716.
[49] VALOVIC, M., BUDNY, R., GARZOTTI, L., et al., Plasma Phys. Controlled Fusion **46** (2004) 1877.
[50] KESSEL, C. E., BUDNY, R. V., and INDIRESHKUMAR, K., Simulation and analysis of the hybrid operating mode in iter, 21st IEEE/NPSS Symposium on Fusion Engineering Knoxville, TN, September 2005.
[51] SNIPES, J. A. and the International H-mode Threshold Database Working Group, Plasma Phys. Controlled Fusion **42** (2000) A299.
[52] SHIMOMURA, Y., MURAKAMI, Y., POLEVOI, A., et al., Plasma Phys. Controlled Fusion **43** (2001) A385.
[53] OLSON, R. E., BERKNER, K. H., GRAHAM, W. G., et al., Phys. Rev. Lett. **41** (1978) 163.
[54] JANEV, R. K., BOLEY, C. D., and POST, D. E., Nucl. Fusion **29** (1989) 2125.
[55] PHANEUF, R. A., JANEV, R. K., and PINDZOLA, M. S., ORNL-6090/V5, Atomic Data for Fusion **5**.
[56] SUZUKI, S., SHIRAI, T., NEMOTO, M., et al., Plasma Phys. Controlled Fusion **40** (1998) 2097.
[57] ANDERSON, H., VON HELLERMANN, M. G., HOCKSTRA, R., et al., Plasma Phys. Controlled Fusion **42** (2000) 781.
[58] OIKAWA, T., USHIGUSA, K., FOREST, C. B., et al., Nucl. Fusion **40** (2000) 435.
[59] NEMOTO, M. and *ET AL.*,, J. Plasma Fusion Res **73** (1997) 1374.
[60] ITER, Design Description Document and Transmission n 53 DDD 31 01-07-10 r0.1 edition .
[61] ITER, Design Description Document and Transmission DDD G 16 35 R0.1 edition .
[62] YUH, H., FOLEY, E., and LEVINTON, F., Conceptual evaluation of measurement of —b(r)— for determination of q(r) on iter, to be submitted to Review of Sci Inst.

Class	$D_{\rm ash}$	$V_{\rm ash}$	$n_{\rm ash}(0)$	$\int dV\ n_{\rm ash}$	$P_{\rm aux}$	$P_{\rm DT}$	$Q_{\rm DT}$
	$[m^2/s]$	$[m/s]$	$[10^{18}/m^3]$	$[10^{21}]$	[MW]	[MW]	
large diffusivity	1.0	+0.1	0.6-1.2	0.3-0.8	53	320	6
small diffusivity	0.1	+0.1	0.2	0.8-3.4	53	320	6
inward pinch	1.0	-1.0	5-19	0.8-3.7	37	170-240	4.6-6.5

Table 1. *Scans of ash transport studied in standard DT plasmas. For all cases, pedestal (boundary) temperatures $\simeq$ 3 keV, 20 MW of He^3 minority heating, $\bar{n}_e/\bar{n}_{\rm GW} = 0.85$, β_n=1.7-1.8, and tight NNBI geometry, were assumed. For the first two cases 33 MW of D-NNBI was assumed. For the inward pinch case 17 MW of D-NNBI was assumed. The definitions of $D_{\rm ash}$ and $V_{\rm ash}$ are given in Eq. 1. Steady state profiles for the second two cases are shown in Figs. 16-a and 17. The pedestal temperature assumption is pessimistic, and other predictions with higher assumed pedestal temperatures, especially in the category of the first class achieve considerably higher $P_{\rm DT}$ and $Q_{\rm DT}$.*

R	$N_{\rm ash}$	$P_{\rm DT}$	$\Gamma_{\rm ash}$	$\tau_{\rm ash}$	$\tau^*_{\rm ash}$	$\tau^*_{\rm ash}$ / $\tau_{\rm E-tot}$
	10^{21}	MW	10^{21}/s	s	s	-
0.95	3.65	160	1.13	3.23	65	22
0.90	2.30	185	0.68	3.38	34	11
0.85	1.74	205	0.50	3.48	23	9
0.80	1.40	215	0.38	3.68	18	6
0.70	1.08	225	0.27	4.00	13	4
0.60	0.88	235	0.19	4.63	12	3

Table 2. *Summary from scan in ash recycling coefficient for the inward pinch case in Table 1. corresponding to results shown in Figs. 16-a and 17. Standard DT plasmas with 17 MW D-NNBI, 20 MW ICRH, $\bar{n}_e/\bar{n}_{\rm GW} = 0.85$, β_n=1.7-1.8. Tight NNBI geometry was assumed. The total stored energy increases from 230 to 250 MJ as R decreases, and the thermal energy confinement time is 2.5-3.0s. The angular momentum confinement time (near $x = 0.85$) is 0.8-1.2 s. The ash confinement time is $\tau_{\rm ash} \equiv N_{\rm ash}/\Gamma_{\rm ash}$.*

RunID units	$B_{\rm TF}$ Tesla	I_p MA	$n_e(0)$ $10^{20}/m^3$	$P_{\rm aux}$ MW	$P_{\rm DT}$ MW	P_e MW	P_i MW	P_α MW	$<\beta_\alpha>$ per cent
20000G05	5.3	15	1.1	53	444	100	40	65	0.12
20100G01	5.3	15	1.1	43	403	95	35	64	0.11
20300G01	4.9	13.8	0.94	53	272	88	27	43	0.095
20200G06	4.3	12	0.84	43	194	65	25	31	0.090

Table 3. *Summary from scan in toroidal field shown in Figs. 22, 23. Standard DT plasmas with $\bar{n}_e/\bar{n}_{\rm GW} = 0.85$, β_n=1.7-1.8, helium ash recycling coefficient R=0.80, tight NNBI geometry, and below-axis steering. The pair of simulations with full field have different $P_{\rm ICRH}(t)$ and slightly different n_e profiles. Run 20300G01 matches 20100G01 with $B_{\rm TF}$, n_e, and I_p scaled down 10%. Run 20200G06 matches 20000G05 with $B_{\rm TF}$, n_e, and I_p scaled down 20%. Values for $P_{\rm aux} \equiv P_{\rm NNBI} + P_{\rm ICRH}$, total electron heating P_e, ion heating P_i, and alpha heating of electrons, $P_{\alpha-el}$ are given in the time window 160-290 s. Computed $P_{\rm DT}$ is approximated by $1.1 \times B^{3.5}$.*

RunID units	I_p MA	β_n	aiming	R	$P_{\rm DT}$ MW	$<\beta_\alpha>$ per cent
20200G01	12	2.1	below axis	0.7	444	0.14
20200G02	12	1.7	below axis	0.7	403	0.08
20200G03	12	1.75	near axis	0.8	272	0.09
20200G04	15	1.45	near axis	0.8	194	0.10

Table 4. *Summary from scan in plasma assumptions with toroidal field reduced 20% to 4.3 T shown in Figs. 24. DT plasmas with 33 MW NNBI, 20MW ICRH, $n_e(0)$=0.84×$10^{20}/m^3$, helium ash recycling coefficient R=0.70-0.80, tight NNBI geometry*

RunID units	$E_{\rm NB}$ keV	$I_{\rm NB}$ kA	$x_{\rm peak}$
20100G21	1000	650	0.14
20100G22	750	600	0.14
20100G23	500	350	0.14
20100G24	250	170	0.15-0.60
20100G25	120	50	0.65

Table 5. *Summary from scan in beam voltage shown in Figs. 25, 26, 27. Standard DT plasmas with 33 MW D-NNBI, $\bar{n}_e/\bar{n}_{\rm GW} = 0.85$, β_n=1.7-1.8. helium ash recycling coefficient R=0.80, tight NNBI geometry, and high steering (to Y=+13cm). The total beam current decreases sharply with decreasing beam energy as the peak ($x_{\rm peak}$) shifts outward and the plasma temperature decreases. Similar shifts are seen in Fig. 25.*

Assumed NNBI geometry	open	tight
tangency radius	5.295	5.295
elevation of ion source	0.60	0.60
ion source half-width	0.291	0.240
ion source half-height	0.68	0.759
distance, ion source to beam aperture	20.8	23.4
distance, ion source to beam tang radius	29.4	30.0
aperture half-width	0.60	0.12
aperture half-height	0.40	0.18
divergence [10^{-3}]	5.0	3.0
focal length [10^{+3}]	$5.0\times10^{+3}$	3.0

Table 6. *Extremes in assumed NNBI geometry are listed. Distances are in [m]. Results presented in this paper use the tight values.*

Species	harmonic	Resonance major radius	heating fraction
		[m]	%
He^3 minority	1	6.70	6.6
T	2	6.70	24.1
D	1	7.59	9.0
He^4	1	7.59	0.5
Ar^{39}_{18}	1	7.93	7.4
Be^9_4	1	8.06	3.4
fast D-NNBI ions	1	7.59	0.6
fast α	1	7.59	0.9
electrons			47.5
T mode conversion	2	6.70	0.0

Table 7. *ICRH power deposition computed by TORIC5 for the simulation 20100G21 at 245s shown in Fig. 35. ICRH frequency = 52MHz, n_{He^3}/n_e assumed to be 0.001.*

Figure Captions

Fig. 1 a) Fusion alpha particles, NNBI, and ICRH heating in a standard H-mode plasma as a function of time. For this case the ICRH power was set to 20 MW early (to help achieve the H-mode, then was ramped down to 12 MW; b) Contributions to the plasma current.

Fig. 2 Densities for the H-mode plasma shown in Fig. 1. Central density evolutions are shown in a) and profiles at 245s (just before a sawtooth crash) are shown in b). The densities of n_e, $n_{\rm Be}$, and $n_{\rm Ar}$ are assumed, while $n_{\rm D}$, $n_{\rm T}$, $n_{\rm ash}$, and $n_{\rm beam}$ are calculated by PTRANSP. A relatively rapid ramp up of density to steady state at 150 s was assumed to permit early (50 s) start of NNBI without excessive shine-through. A modified Kadomstev sawtooth mixing is assumed with a sawtooth period of 50 s.

Fig. 3 The electron and ion temperatures in an H-mode plasma shown in Figs. 2 and 1. The temperatures at the top of the pedestal ($x = 0.9$) are assumed while the remainder of the temperature profiles are calculated using the GLF23 and NCLASS models, together with computed heat sources and sinks.

Fig. 4 DT neutron emission rate and corresponding $P_{\rm DT}$ as a function of time produced in the H-mode plasma shown in the previous figures. It is shown that the thermonuclear emission dominates. The beam-target emission is also shown. The NNBI is D, so there is no direct beam-beam DT emission. The conversion from DT neutrons per sec to MW is $3.6{\times}10^{17}$ MW/neutron. The heating power (shown in Fig. 1) is ramped up to 53, then down to 45 and finally 33 MW. This simulation achieves corresponding $P_{\rm DT}$ = peaking at 430, then dropping to 405 and then 390 MW, so the $Q_{\rm DT}$ increases from 8.1 to 9.0, then 11.8.

Fig. 5 Profile at 245 s (just before a sawtooth crash) of a) NNBI beam density and b) normalized pressure $\beta_{\rm beam}$ in standard H-modes with different steering. Y [cm] is the height of the center of the beam measured from the vessel midplane. The present plans for the ITER NNBI allow for variation of Y between +15 and -42 cm so the most central aiming shown at $Y = +38$ cm would not be possible. The predicted magnetic axis is elevated to $Y = 53$ cm.

Fig. 6 Profiles of $-R\nabla(\beta_{beam})$ with differing NNBI steering and of $-R\nabla(\beta_\alpha)$ which is nearly independent of NNBI steering.

Fig. 7 Profiles of a) NNBI-induced currents; b) total currents at a quasi-steady state time just

before a sawtooth break predicted for standard H-mode plasmas with different beam steering (shown in Fig. 5).

Fig. 8 Magnetic q profiles in standard H-mode plasmas with different beam steering (shown in Figs. 5,7) at a quasi-steady state time just before a sawtooth break. The values in the inner half ($x < 0.5$) are weakly effected by steering, but are strongly effected by sawtooth mixing discussed later.

Fig. 9 Evolution of the total current density profile and q profiles associated with a sawtooth crash.

Fig. 10 Predicted beam density profile (left panel) and central q as a function of time (right panel) with two beam steering angles. The Porcelli model is used to trigger sawtooth crashes.

Fig. 11 Time evolution of the central q value between sawtooth crashes in standard H-mode plasmas (shown in Figs. 5,7,8) with 50 s sawtooth periods and a variety of different NNBI steering angles.

Fig. 12 Profiles of predicted redistribution of the fast alpha density profiles (left panel) and fast beam density profile (right panel) during a short time interval around a sawtooth crash occurring at 300.5 s. Regeneration of density in the core starts soon after the crash. Effects of Monte Carlo noise are seen in the profiles.

Fig. 13 Profiles of a) predicted NNBI-torque, and b) induced rotation in the plasmas shown in Figs. 5,7,8, and 11) with different NNBI steering angles. The ion transport is computed using $\chi_\phi = \chi_i$.

Fig. 14 Profile of E_r predicted by radial force balance and the predicted toroidal rotation from NNBI and the poloidal rotation from the NCLASS neoclassical model, (Ref. [28]). The $v_{tor}B_{pol}$, $v_{pol}B_{tor}$, and ∇(pressure) terms are shown.

Fig. 15 a) Profiles of predicted toroidal rotation frequency computed using different ratios of χ_ϕ/χ_i and computed using χ_ϕ from the GLF23 model. b) Ion temperature profiles at 245 s predicted using GLF23 with flow shear stabilization and different ratios of χ_ϕ/χ_i.

Fig. 16 Simulations of ash density profiles from thermalization of fusion alpha particles and wall recycling in a DT H-mode with 17 MW NNBI and 20 MW ICRH. Two assumptions for the ash

transport are used. a) assuming an inward pinch; b) assuming a small diffusivity and an outward pinch. The values of $D_{\rm ash}$ and $V_{\rm ash}$ are summarized in Table 1. Different values of the ash recycling coefficient R are assumed.

Fig. 17 Simulations of number of ash ions and $P_{\rm DT}$ from thermalizing fusion alpha particles and wall recycling in a DT H-mode plasmas with 17 MW NNBI and 20 MW ICRH, corresponding to the inward pinch case in Fig. 16. The case $R = 0.6$ achieves $P_{\rm DT}$=235 MW. The $P_{\rm DT}$ is reduced to 155 MW if R=0.95 due to dilution of the D and T fuel (at fixed n_e. The number of He ash ions are shown in the left panel and the DT neutron emission rates are shown in the right panel. The resulting $P_{\rm DT}$, ash confinement times τ_p, and $\tau_p^* \equiv \tau_p/(1-R)$ are summarized in Table 2.

Fig. 18 Profiles of T_i and T_e predicted for DT H-mode plasmas with 33 MW D-NNBI and 20 MW ICRH and with differing assumptions for the pedestal temperature. The boundary temperatures for GLF23 were set at $x = 0.95$ with values 0.5, 2.9, and 4.6 keV. The simulations predict $P_{\rm DT}$ values of 100, 245, and 445 MW, and $Q_{\rm DT}$ flattop values of 1.9, 4.7, and 8.8.

Fig. 19 Simulation of a DT plasma with mildly peaked n_e profiles. A slow ramp up to steady state at 200 s was assumed, with 17 MW D-NNBI and 20 MW ICRH ICRH ramping up from 60 to 100 s. The ash recycling was assumed to be $R = 0.8$. The fusion power $P_{\rm DT}$ is 140 MW. Predictions of neutron emission with two assumptions of the sawtooth period and with different steering are shown in 19-b. The central ion temperatures are relatively high during the low density phase, and then drop to approximately 15 keV if the sawtooth period is long. They are about 1 keV lower with the fast sawteeth predicted by the Porcelli model.

Fig. 20 Profiles of T_e and T_i predicted for H-mode plasmas using only the first isotope of hydrogen. The heating is assumed to be 8 MW H-NNBI at 500 keV and 20 or 40 MW He^3 minority ICRH.

Fig. 21 Neutron emission rates predicted for a D-only H-mode. The heating is assumed to be 17 MW D-NNBI at 1 MeV and 40 MW He^3 minority ICRH. The Porcelli model was used to predict sawteeth crashes.

Fig. 22 Electron temperature T_e predicted for a scan in $B_{\rm TF}$: a) central T_e; b) profiles at 245 s (just before a sawtooth crash). Plasma conditions are summarized in Table 3.

Fig. 23 Ion temperature T_i predicted for a scan in $B_{\rm TF}$ (with He recycling coefficient $R = 0.8$): a)

central T_i; b) profiles at 245s (just before a sawtooth crash). Plasma conditions are summarized in Table 3.

Fig. 24 Predicted T_i with $B_{\rm TF}$ reduced 20% and scan in NNBI aiming, pedestal temperature (increasing β_n from 1.7 to 2.1), and I_p (from 12 to 15 MA, changing q). Plasma conditions are summarized in Table 4.

Fig. 25 a) Predicted NNBI deposition on thermal D, T ions as $E_{\rm NNBI}$ is reduced from 1 MeV to 120 keV. The NNBI steering is high (Y=13cm). The full-energy current fraction is assumed to be 100% for all except the 120keV case. For the latter, the full-energy current fraction is assumed to be 40%. b) Predicted NNBI shine-through for the scan in beam energy. The highest curve corresponds to the case shown in Fig. 1b) with excited-states ionization. The total power decreases rapidly with decreasing beam energy. Plasma conditions are summarized in Table 5.

Fig. 26 NNBI total torque profiles for the scan in beam energy. a) PTRANSP profile averaged over 25 s to reduce Monte Carlo noise, b) Volume-integrated NNBI total torque for the scan in beam energy. The total torque is doubled for 33 MW at 120 keV compared with 33 MW at 1 MeV. Plasma conditions are summarized in Table 5.)

Fig. 27 Predictions of toroidal rotation frequency profiles for the scan in beam energy. The momentum transport is assumed to be related to the thermal ion transport by $\chi_\phi = \chi_i$. Plasma conditions are summarized in Table 5.)

Fig. 28 Examples of pressure profiles for a standard H-mode with 33 MW D-NNBI at 1 MeV at 245 s (before a sawtooth crash). The pressure of the beam ions from below-axis NNBI causes the MHD pressure $P_{\rm MHD}$ to peak off axis. The smoothing option and $P_{\rm MHD-smoothed}$ were used by TEQ. The profile $P_{\rm check}$ is the solution to the Grad-Shafranov equation in 1D.

Fig. 29 Example of the error in a TEQ equilibrium solution for the standard H-mode prediction shown in Fig. 12, 12-28. The error is defined by the absolute value of the difference between the two sides of the Grad-Shafranov equation divided by the area-average of the plasma current side.

Fig. 30 Predicted beam deposition profiles for a standard H-mode with 33 MW D-NNBI at 1 MeV. The total profile is the sum of ionization on thermal ions, impurities, electrons, beam-beam interactions internal and charge-exchange, and charge-exchange on thermal T and D. The charge-exchange on the He^4 ash is relatively low and not shown.

Fig. 31 Comparisons of predictions with and without the multi-state ionization cross sections of a) profile of the rate of ionization on hydrogen plasma; b) total shine-through power. The ramp up of $n_e(0)$ is shown for comparison with values of the projected $P_{\rm LH}$. Reference [44] suggest that $P_{\rm LH}$ will be 52 MW at $n_e(0) = 5 \times 10^{19}/{\rm m}^3$ and increase to 86 MW at $n_e(0) = 10^{20}/{\rm m}^3$. If $P_{\rm LH}$ scales as $2/A$ ([45]) then these threshold powers would be twice as high.

Fig. 32 Sensitivity of total shine-through power to uncertainties in the atomic cross sections assuming 10 MW H-NNBI at 870keV into into H-plasma while the density is ramped up. The GLF23-predicted temperatures are insensitive to these assumptions.

Fig. 33 Examples of NNBI neutral trajectories with below-midplane steering; a) poloidal plane projection; b) top view with injection in the co (I_p) direction.

Fig. 34 Examples of profiles of NNBI-torques (smoothed over 50s): collisional torque $t_{\rm bco}$; j $\times$ B torque $t_{\rm j\times B}$; and beam thermalization torque $t_{\rm bth}$.

Fig. 35 Examples of ICRH results computed by the TORIC module in PTRANSP for the H-mode prediction shown in Fig. 12, 12-29. The He^3 concentration was assumed to be 0.1% of the electron density. For this case, the toroidal wavenumber was assumed to be $n_\phi = 27$. Contours of the real part of E_+ in a section at fixed toroidal angle. The TORIC coordinate system is centered at the magnetic axis.

Fig. 36 Profiles of of power depositions for the TORIC run shown in Fig. 35 averaged over x $\equiv$ square-root of the normalized toroidal flux. Note that the power deposition on fast beam and alpha ions is relatively small. A summary of total powers is given in Table 7.

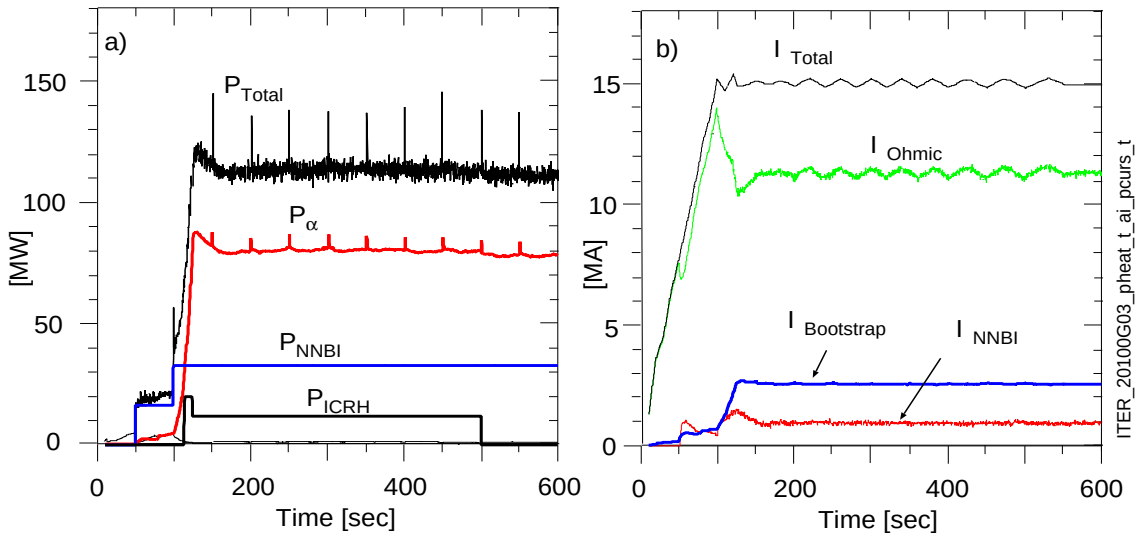

Figure 1.

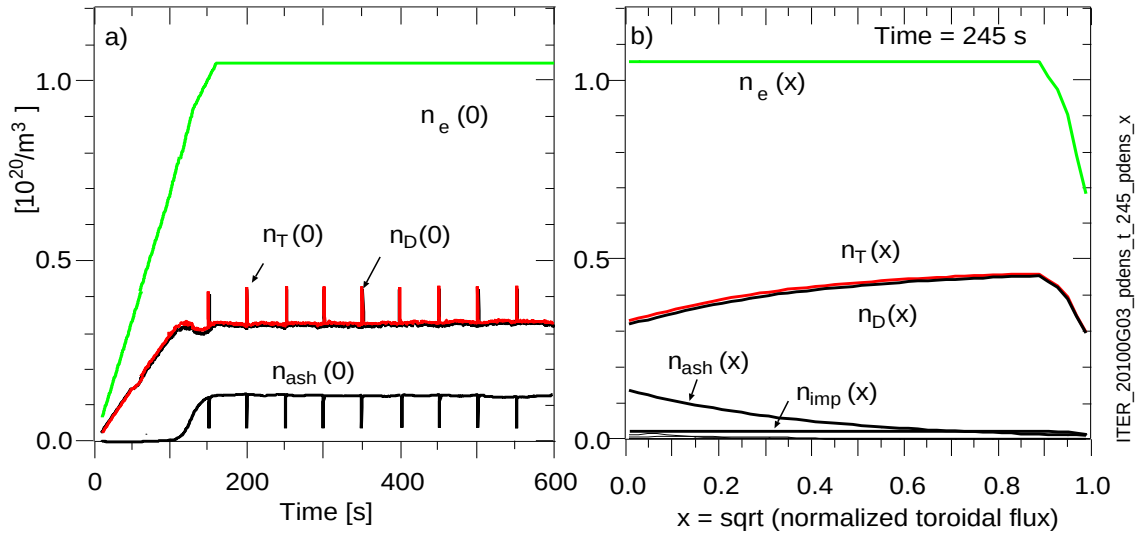

Figure 2.

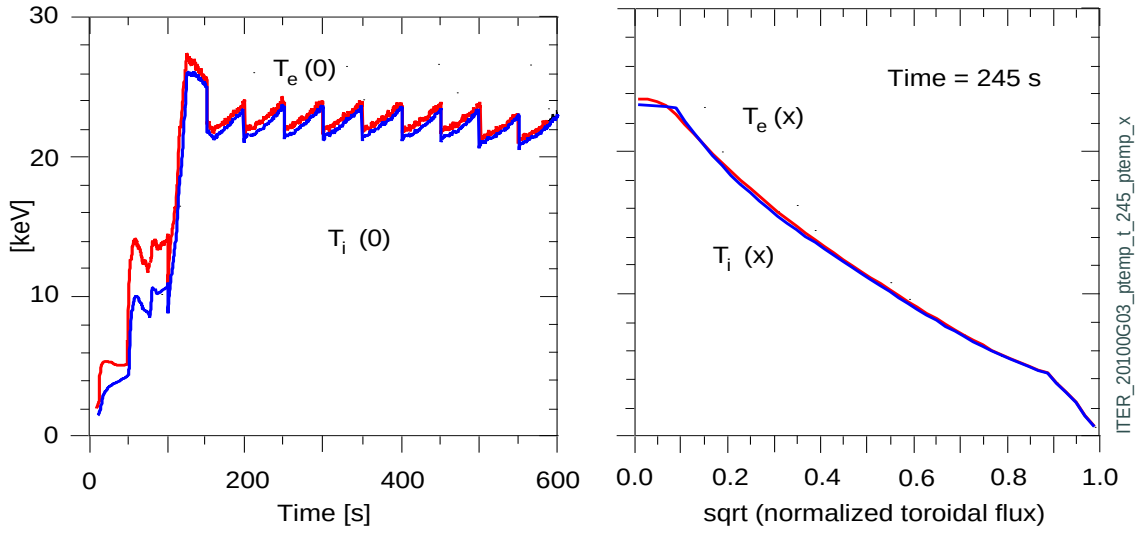

Figure 3.

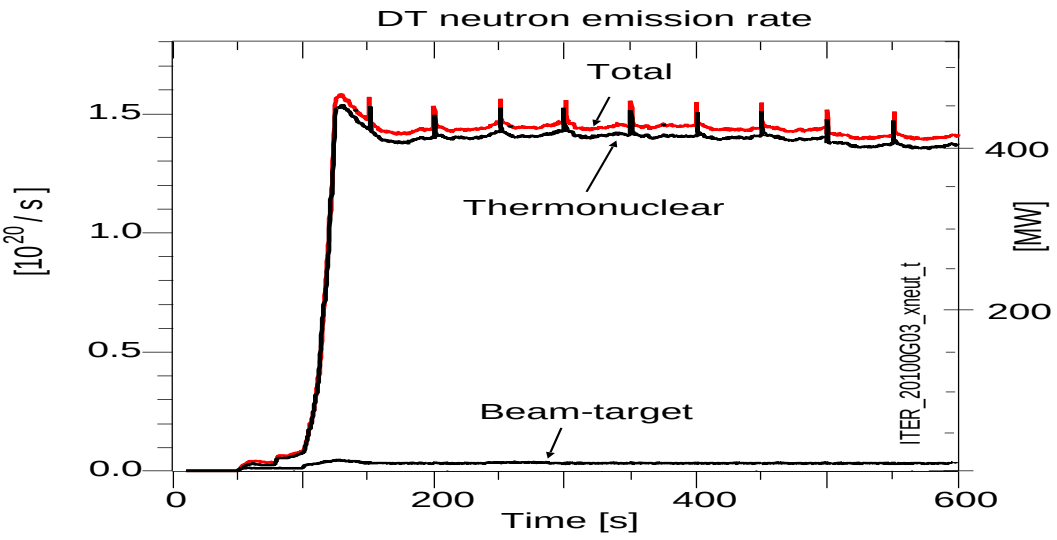

Figure 4.

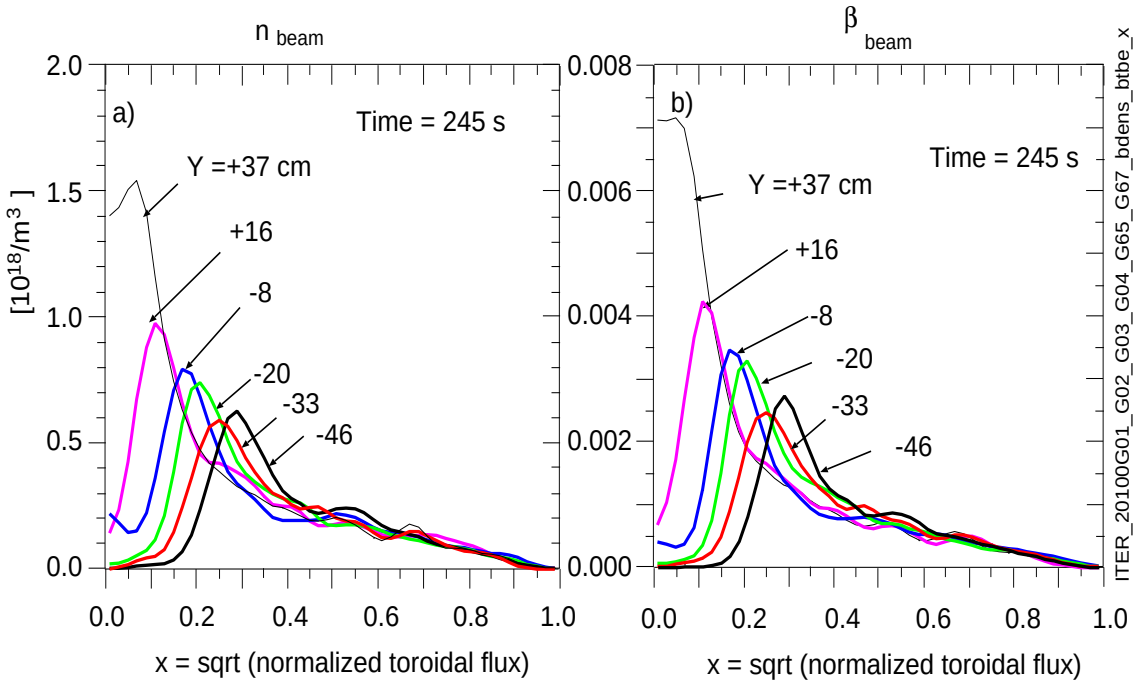

Figure 5.

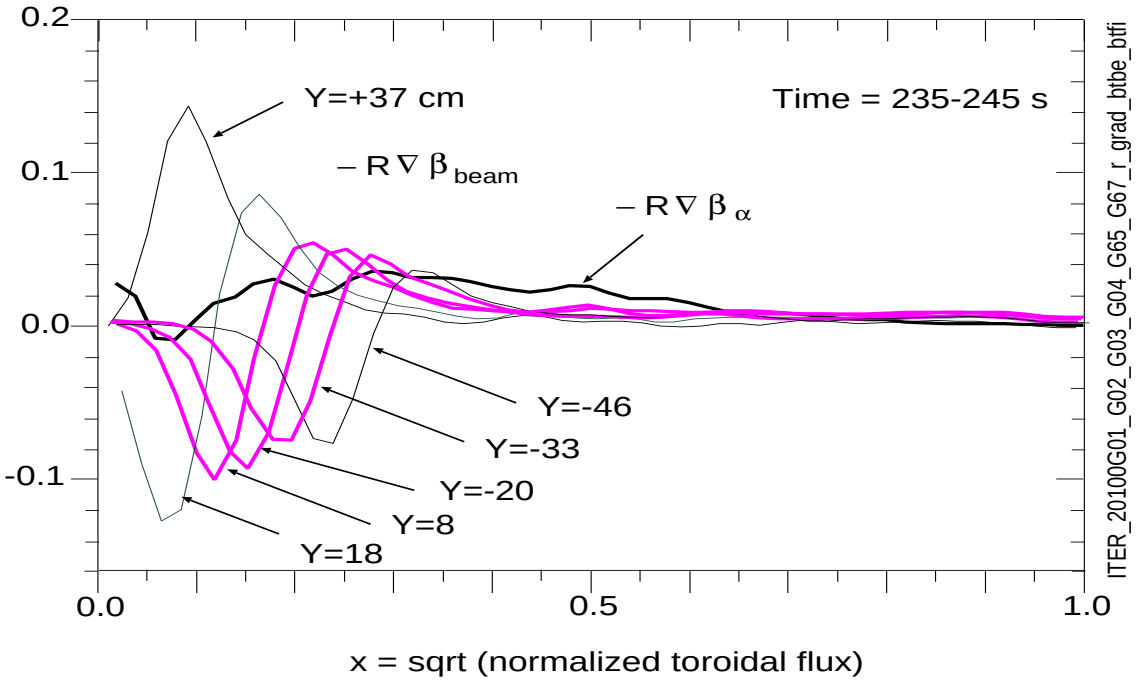

Figure 6.

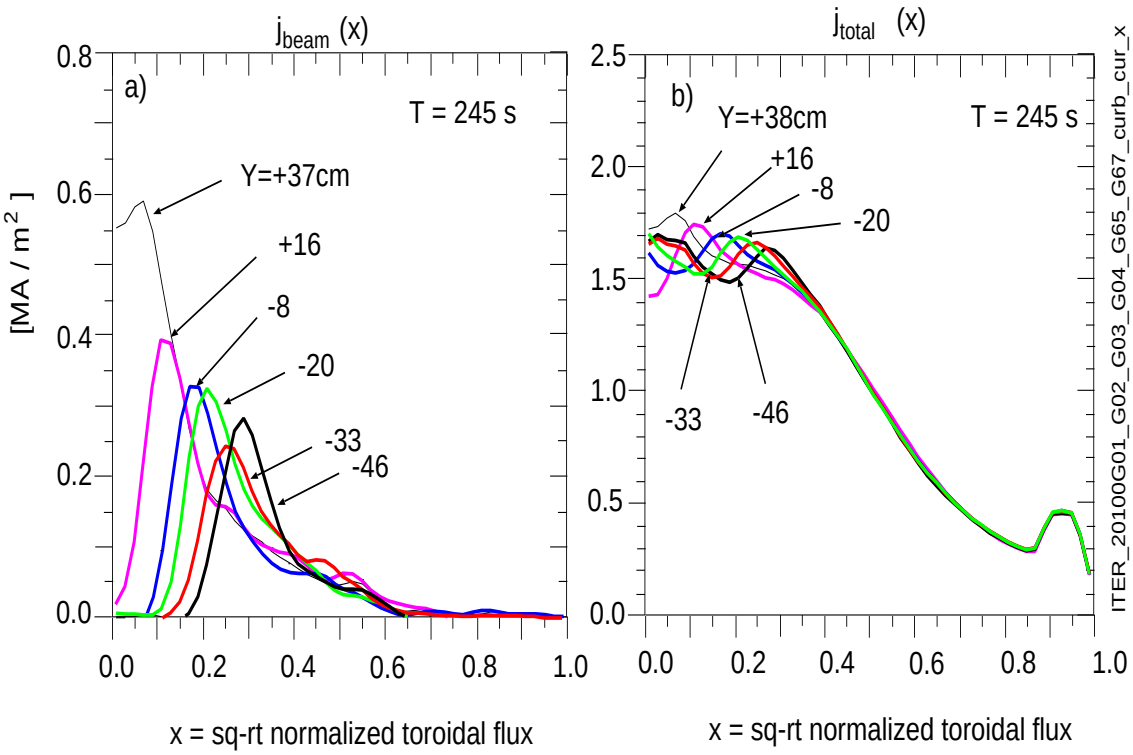
j_beam (x)
a)
T = 245 s
Y=+37cm
+16
-8
-20
-33
-46
[MA / m^2]
0.0
0.2
0.4
0.6
0.8
1.0
x = sq-rt normalized toroidal flux
j_total (x)
b)
Y=+38cm
T = 245 s
+16
-8
-20
-33
-46
0.0
0.5
1.0
1.5
2.0
2.5
x = sq-rt normalized toroidal flux
ITER_20100G01_G02_G03_G04_G65_G67_curb_cur_x

Figure 7.

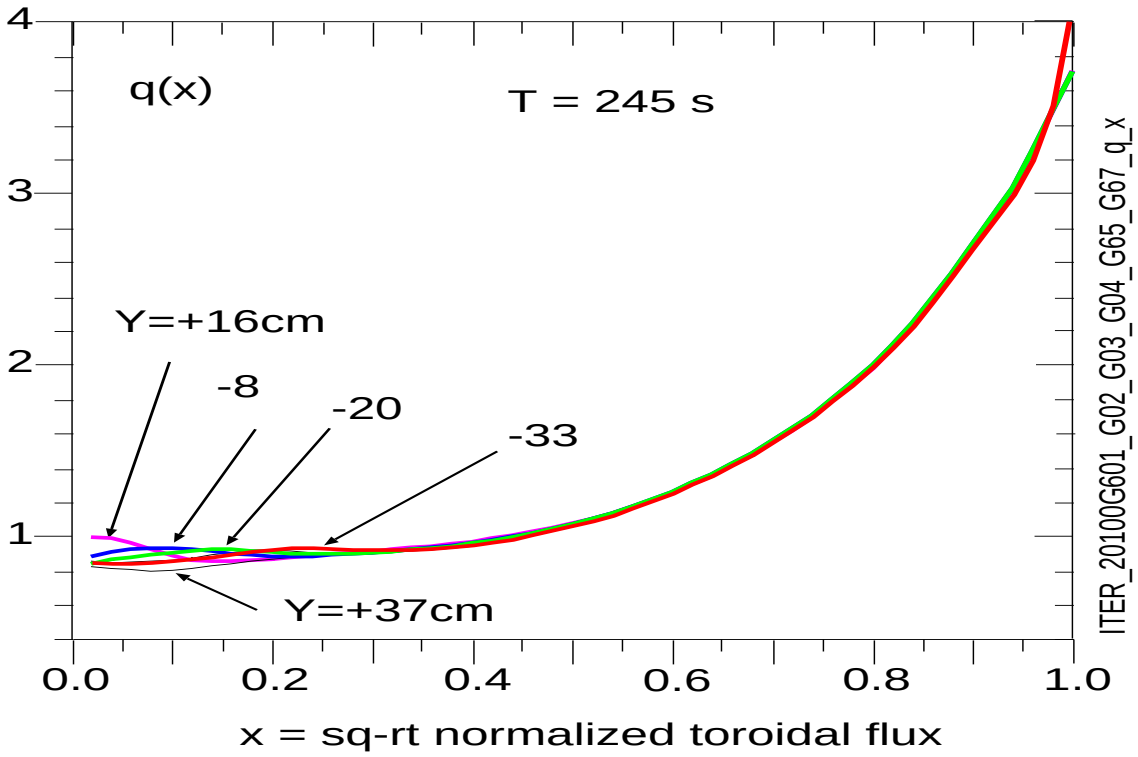
q(x)
T = 245 s
Y=+16cm
-8
-20
-33
Y=+37cm
4
3
2
1
0.0
0.2
0.4
0.6
0.8
1.0
x = sq-rt normalized toroidal flux
ITER_20100G601_G02_G03_G04_G65_G67_q_x

Figure 8.

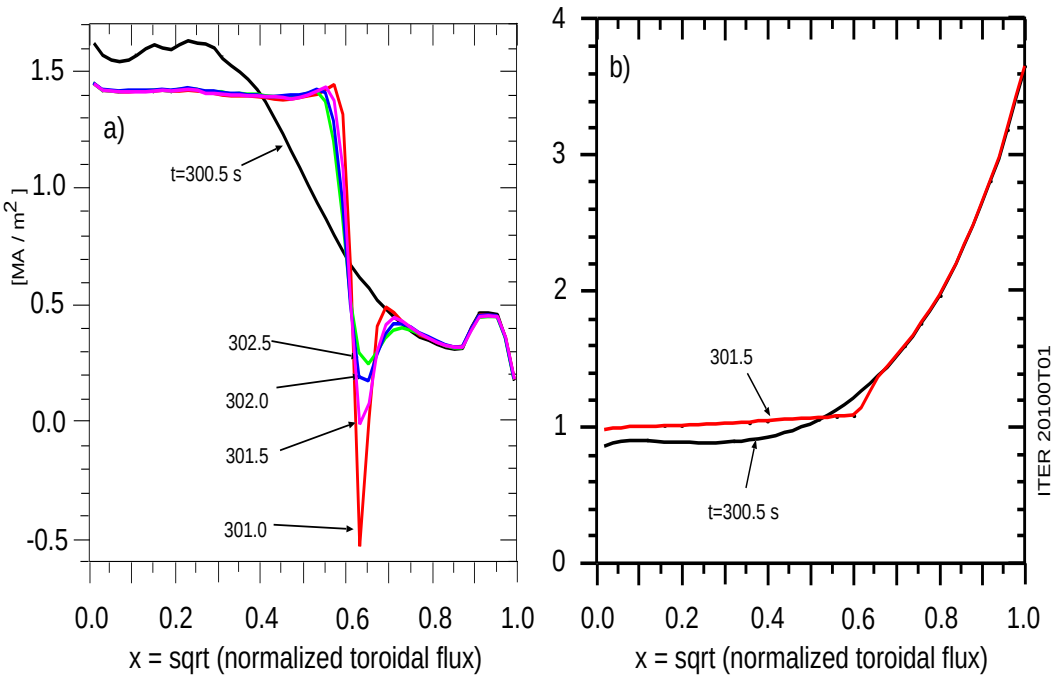

Figure 9.

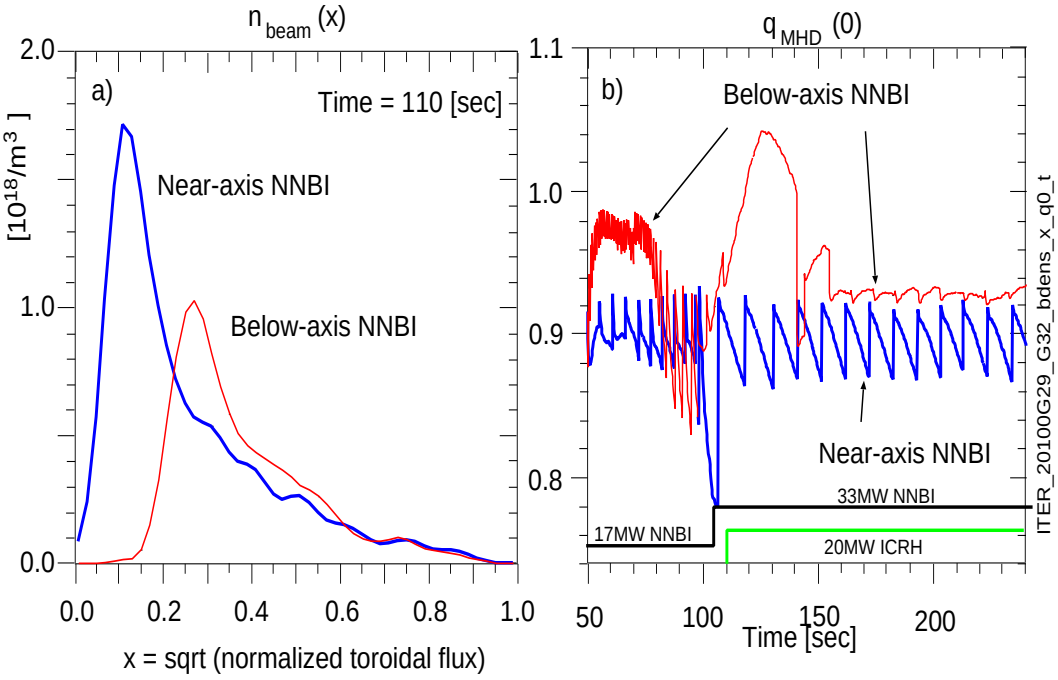

Figure 10.

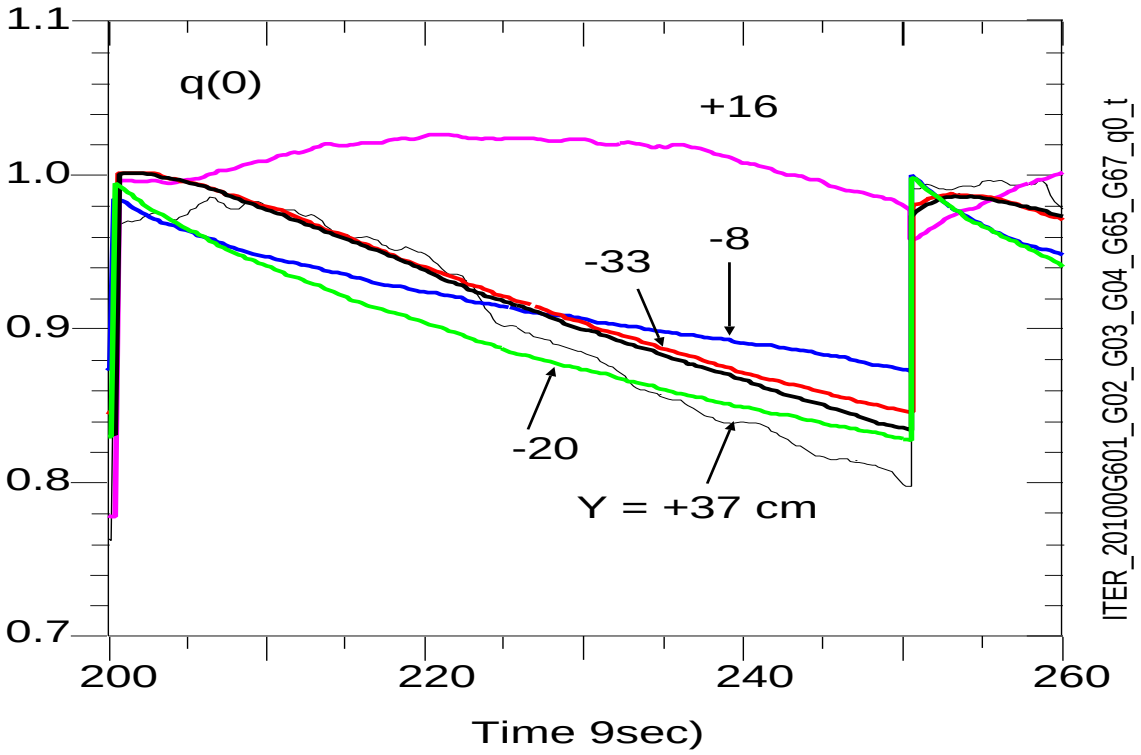
1.1
1.0
0.9
0.8
0.7
q(0)
+16
-8
-33
-20
Y = +37 cm
200
220
240
260
Time 9sec)
ITER_20100G601_G02_G03_G04_G65_G67_q0_t

Figure 11.

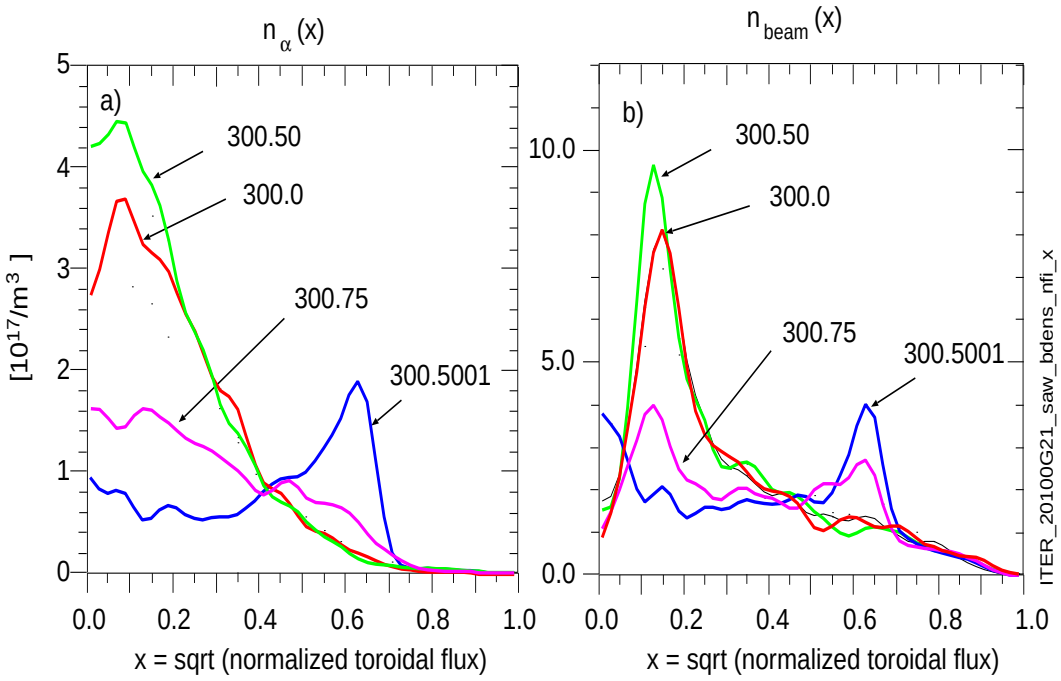

Figure 12.

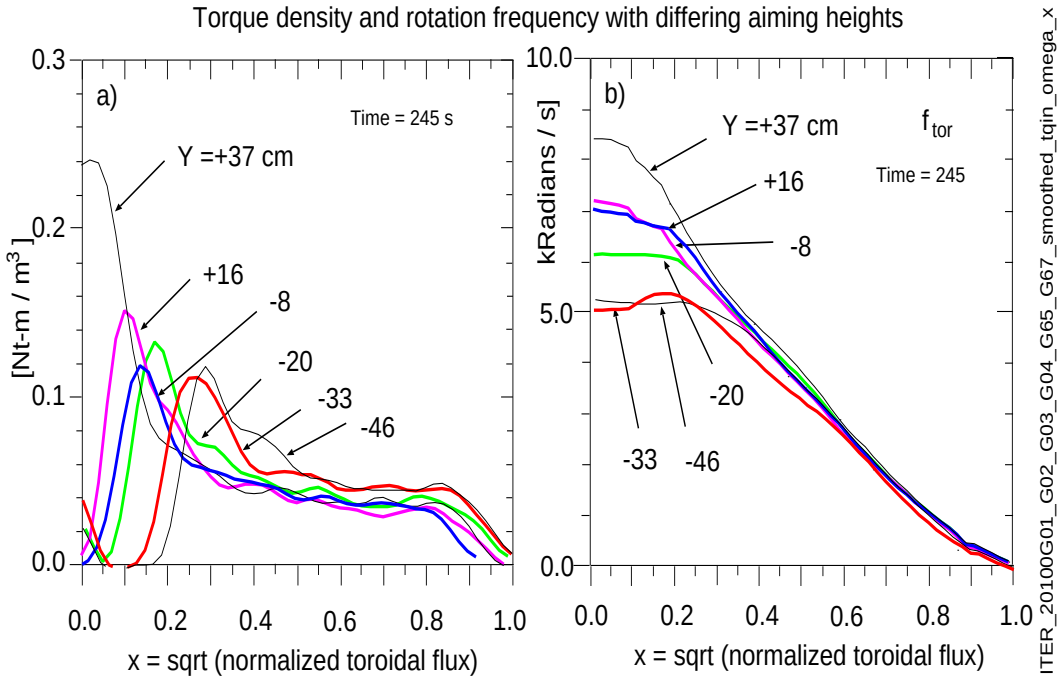

Figure 13.

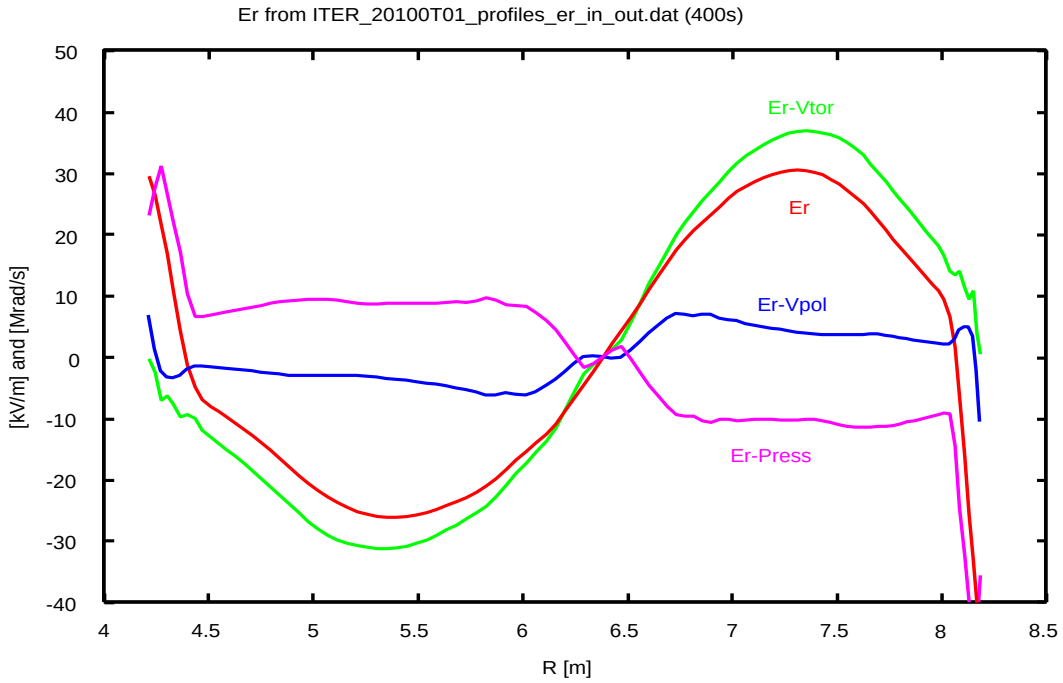

Figure 14.

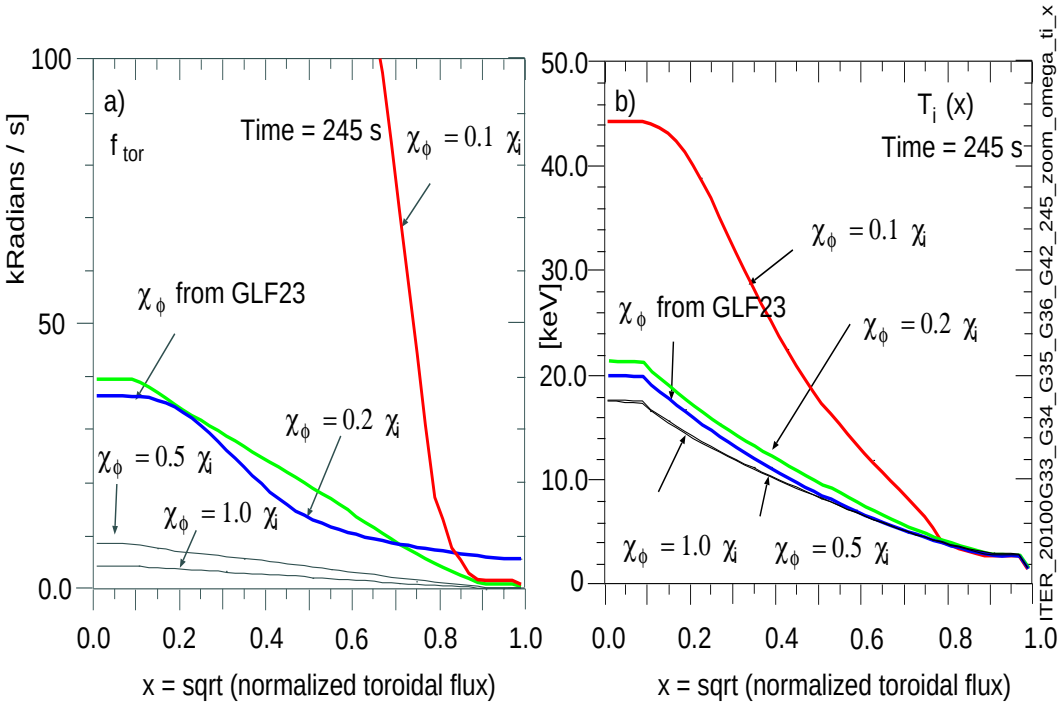

Figure 15.

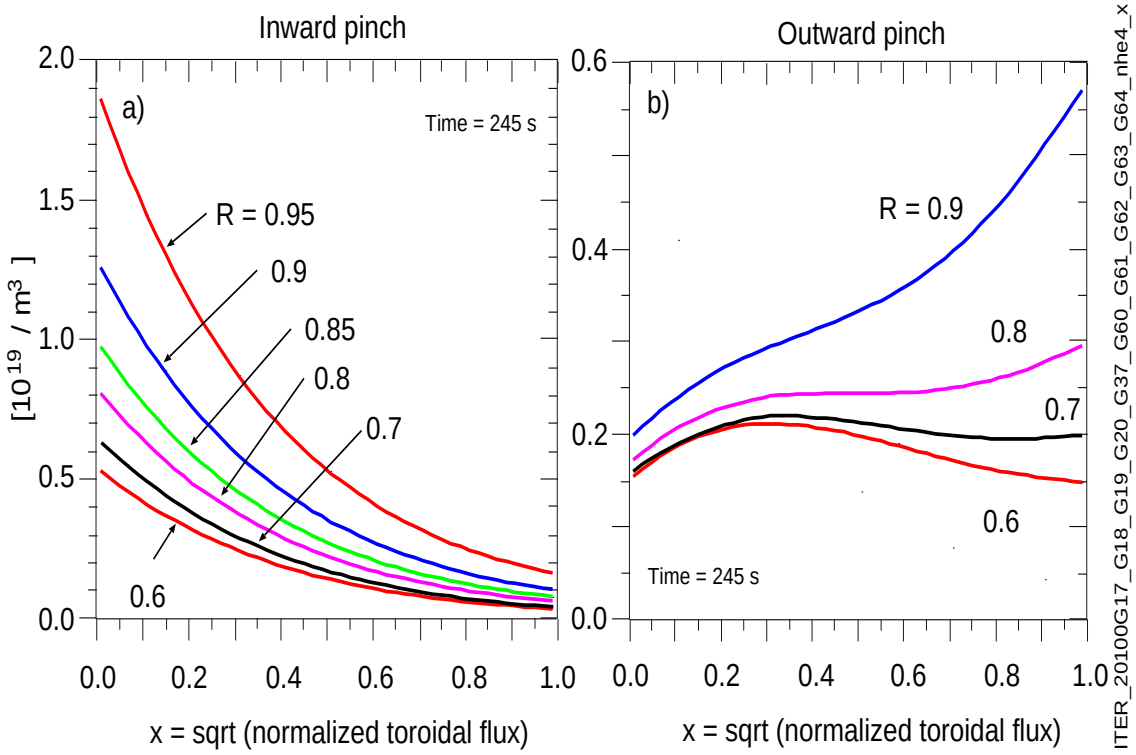
Inward pinch
Outward pinch
a)
b)
Time = 245 s
Time = 245 s
R = 0.95
0.9
0.85
0.8
0.7
0.6
R = 0.9
0.8
0.7
0.6
[10^19 / m^3]
x = sqrt (normalized toroidal flux)
x = sqrt (normalized toroidal flux)
ITER_20100G17_G18_G19_G20_G37_G60_G61_G62_G63_G64_nhe4_x

Figure 16.

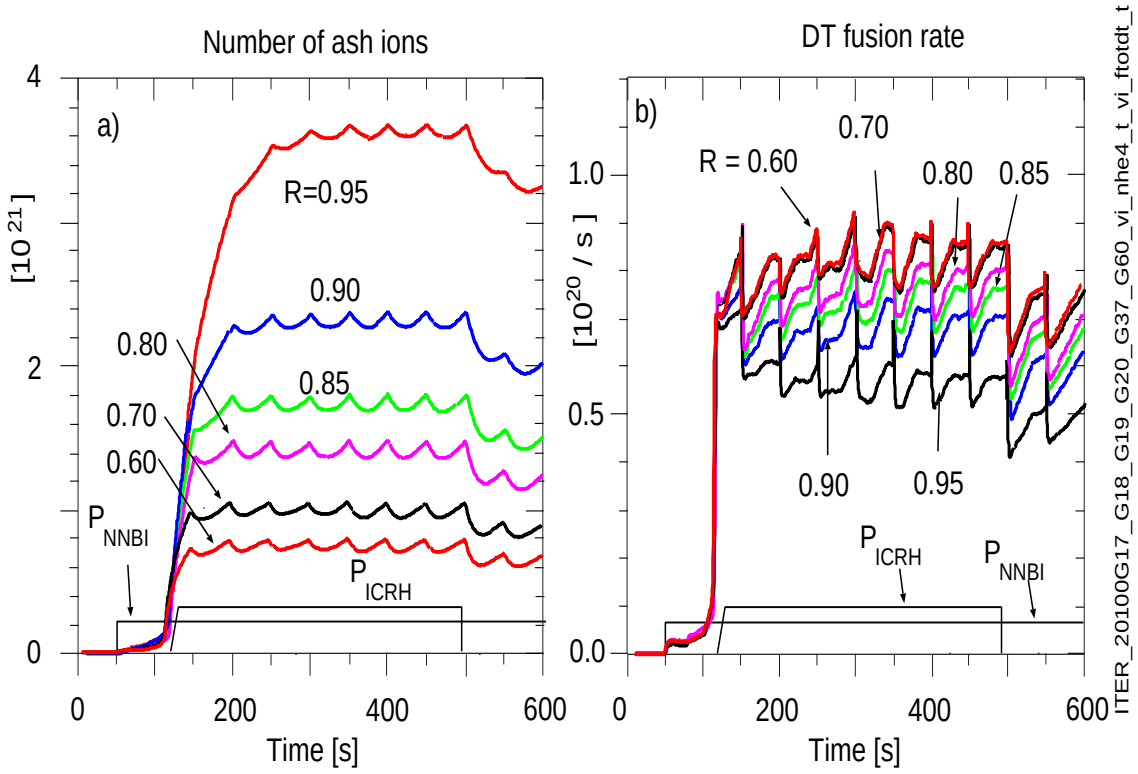
Number of ash ions
a)
R=0.95
0.90
0.80
0.85
0.70
0.60
P NNBI
P ICRH
[10 21]
Time [s]
DT fusion rate
b)
0.70
R = 0.60
0.80
0.85
0.90
0.95
P ICRH
P NNBI
[10 20 / s]
Time [s]
ITER_20100G17_G18_G19_G20_G37_G60_vi_nhe4_t_vi_ftotdt_t

Figure 17.

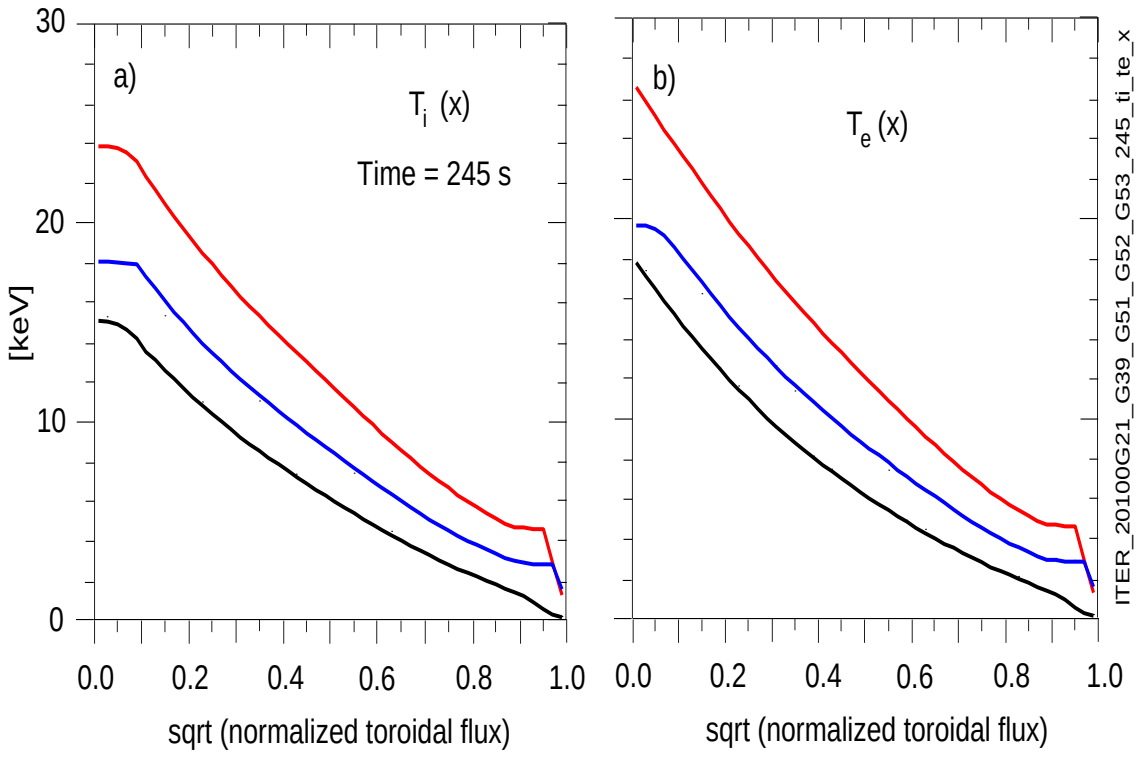
a)
T_i (x)
Time = 245 s
[keV]
30
20
10
0
0.0
0.2
0.4
0.6
0.8
1.0
sqrt (normalized toroidal flux)
b)
T_e (x)
sqrt (normalized toroidal flux)
ITER_20100G21_G39_G51_G52_G53_245_ti_te_x

Figure 18.

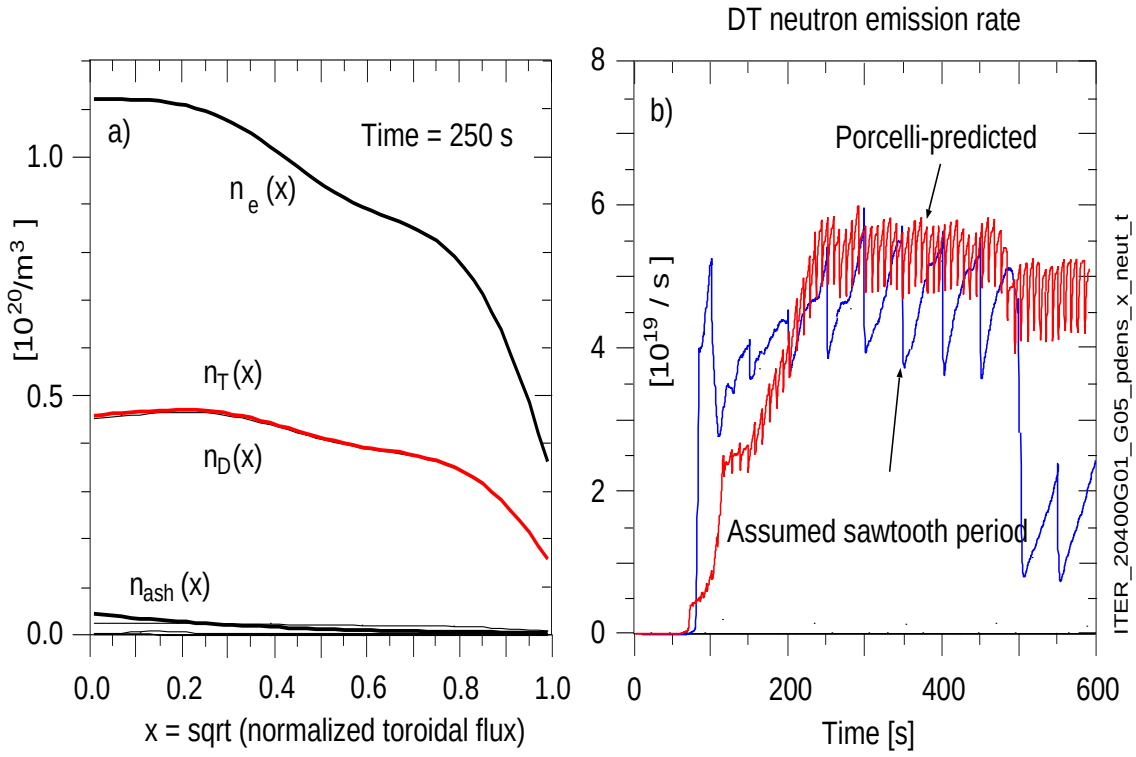
a)
Time = 250 s
n e (x)
nT (x)
nD(x)
nash (x)
[10^20/m^3]
1.0
0.5
0.0
0.0
0.2
0.4
0.6
0.8
1.0
x = sqrt (normalized toroidal flux)
DT neutron emission rate
b)
Porcelli-predicted
Assumed sawtooth period
[10^19 / s]
8
6
4
2
0
0
200
400
600
Time [s]
ITER_20400G01_G05_pdens_x_neut_t

Figure 19.

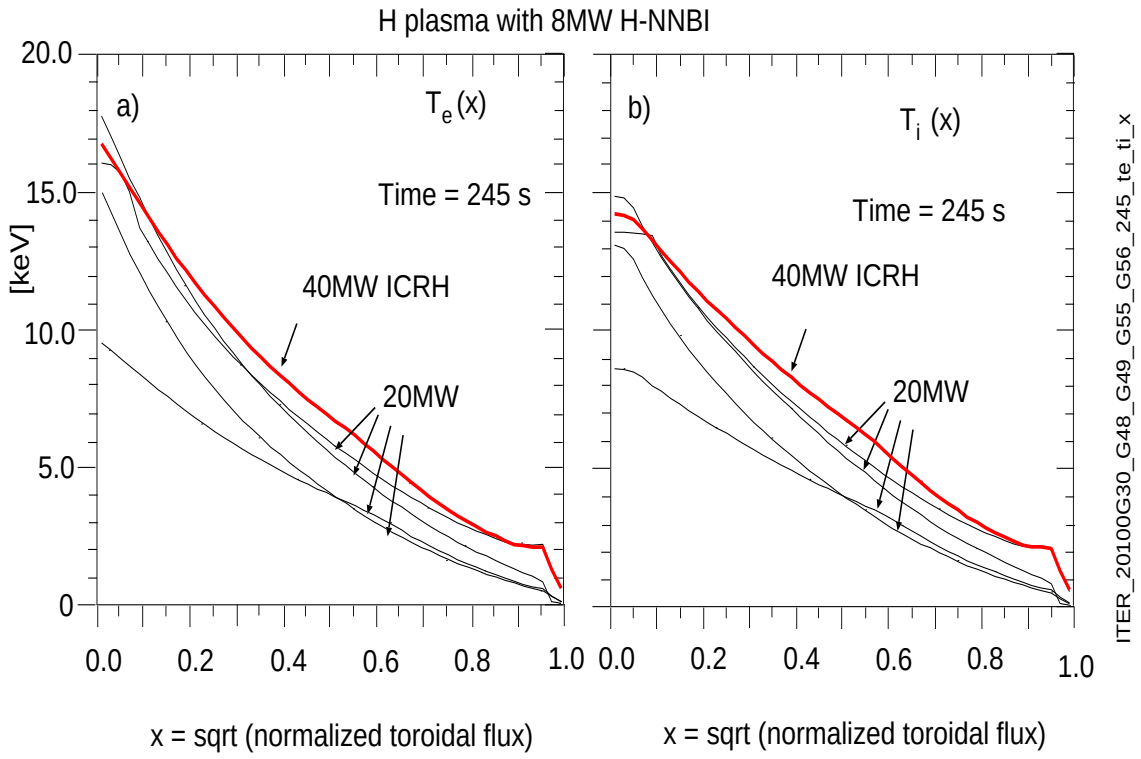
H plasma with 8MW H-NNBI
a)
T_e (x)
Time = 245 s
40MW ICRH
20MW
[keV]
20.0
15.0
10.0
5.0
0
0.0
0.2
0.4
0.6
0.8
1.0
x = sqrt (normalized toroidal flux)
b)
T_i (x)
Time = 245 s
40MW ICRH
20MW
x = sqrt (normalized toroidal flux)
ITER_20100G30_G48_G49_G55_G56_245_te_ti_x

Figure 20.

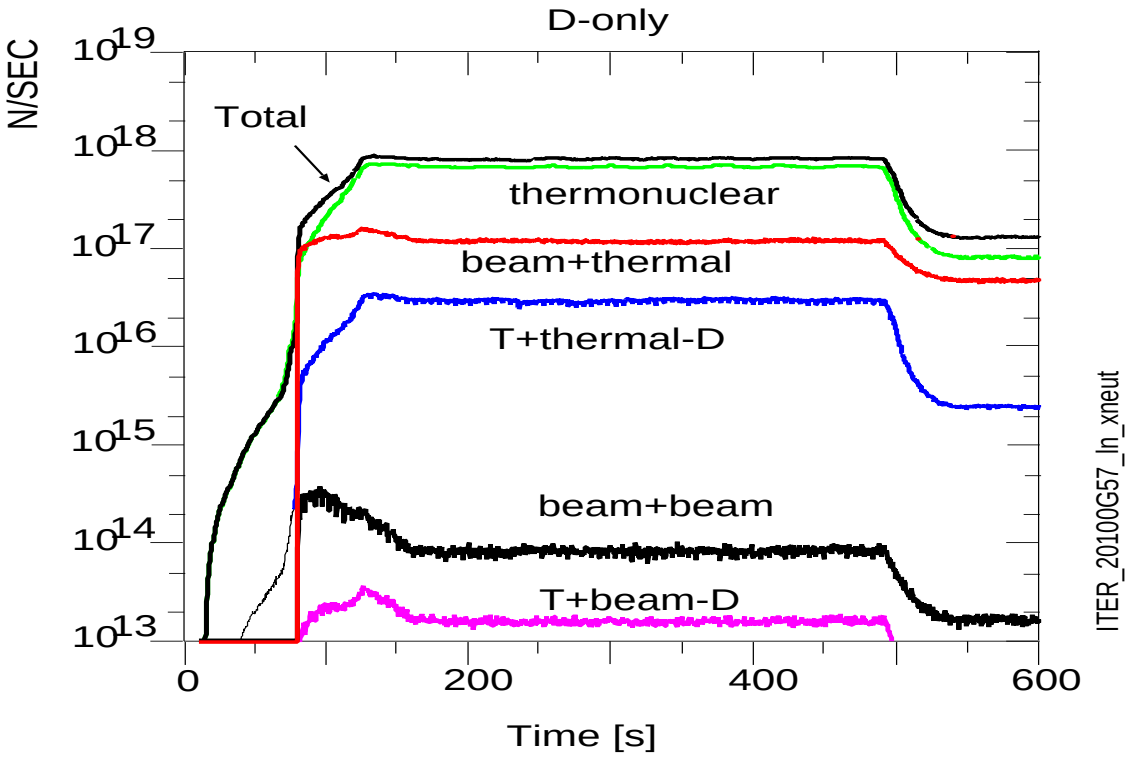
D-only
N/SEC
10^{19}
10^{18}
10^{17}
10^{16}
10^{15}
10^{14}
10^{13}
Total
thermonuclear
beam+thermal
T+thermal-D
beam+beam
T+beam-D
0
200
400
600
Time [s]
ITER_20100G57_ln_xneut

Figure 21.

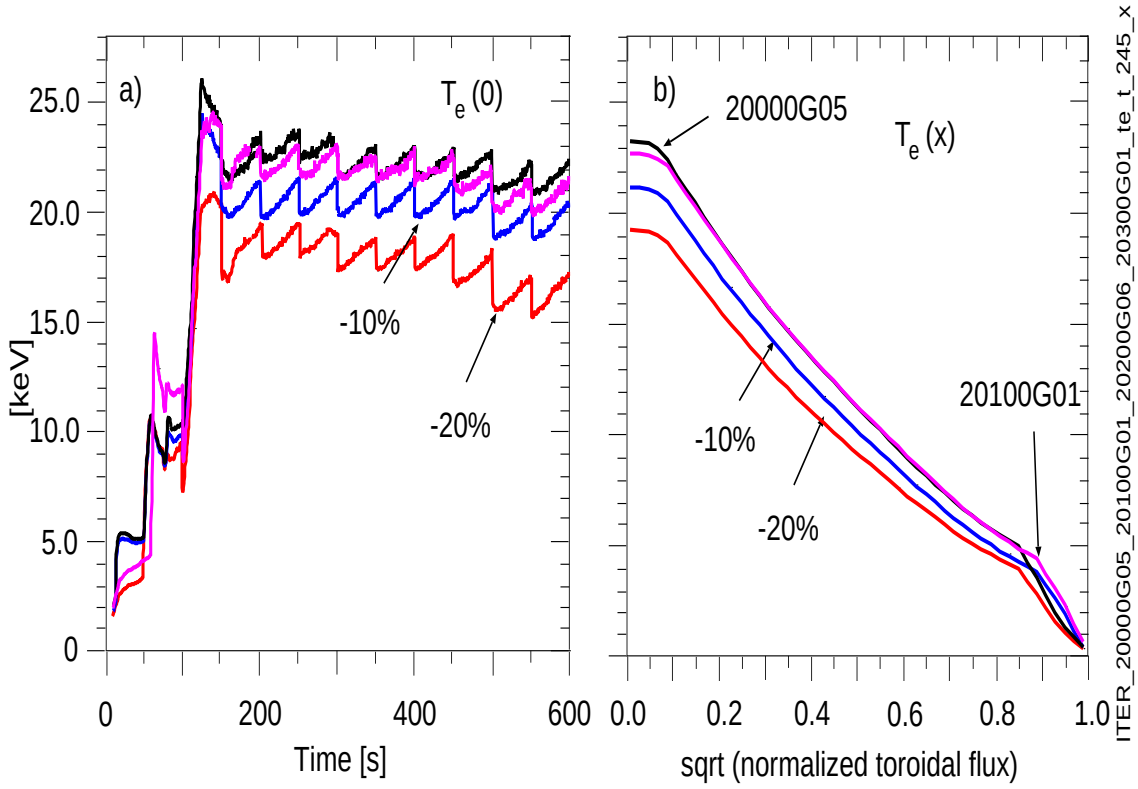
a)
T_e (0)
-10%
-20%
[keV]
25.0
20.0
15.0
10.0
5.0
0
0
200
400
600
Time [s]
b)
20000G05
T_e (x)
20100G01
-10%
-20%
0.0
0.2
0.4
0.6
0.8
1.0
sqrt (normalized toroidal flux)
ITER_20000G05_20100G01_20200G06_20300G01_te_t_245_x

Figure 22.

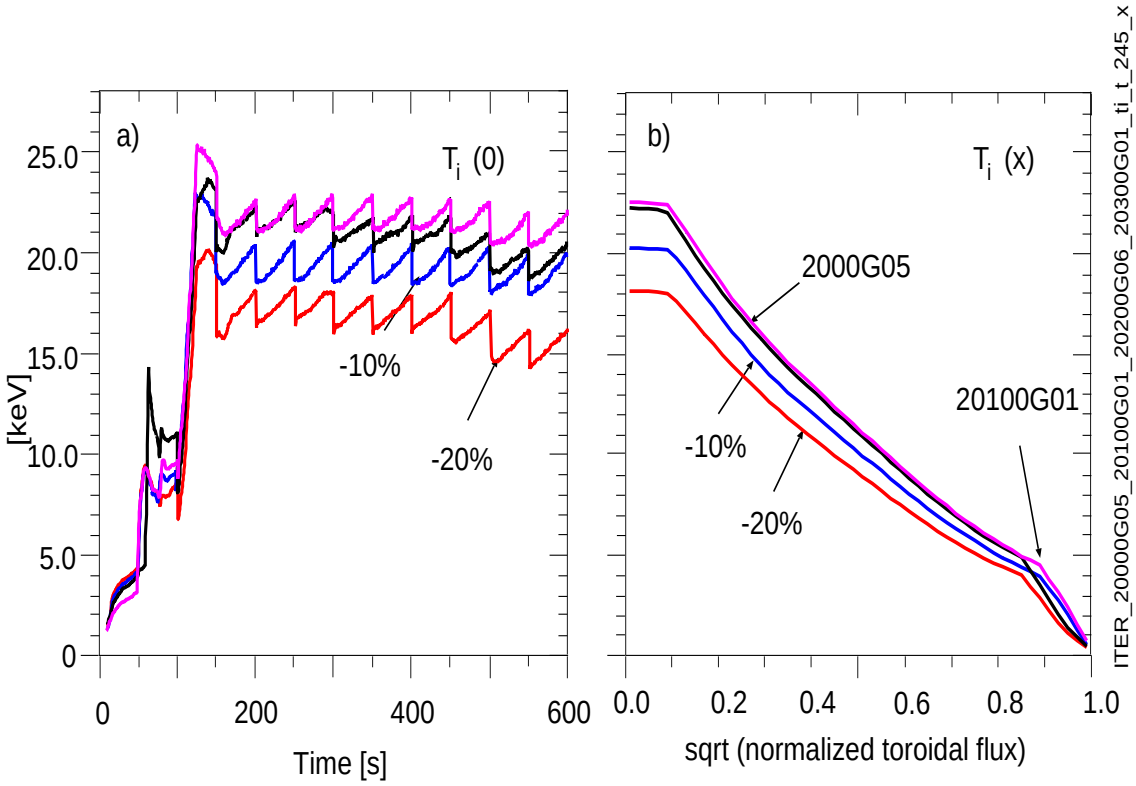
a)
T_i (0)
-10%
-20%
[keV]
25.0
20.0
15.0
10.0
5.0
0
0
200
400
600
Time [s]
b)
T_i (x)
2000G05
20100G01
-10%
-20%
0.0
0.2
0.4
0.6
0.8
1.0
sqrt (normalized toroidal flux)
ITER_20000G05_20100G01_20200G06_20300G01_ti_t_245_x

Figure 23.

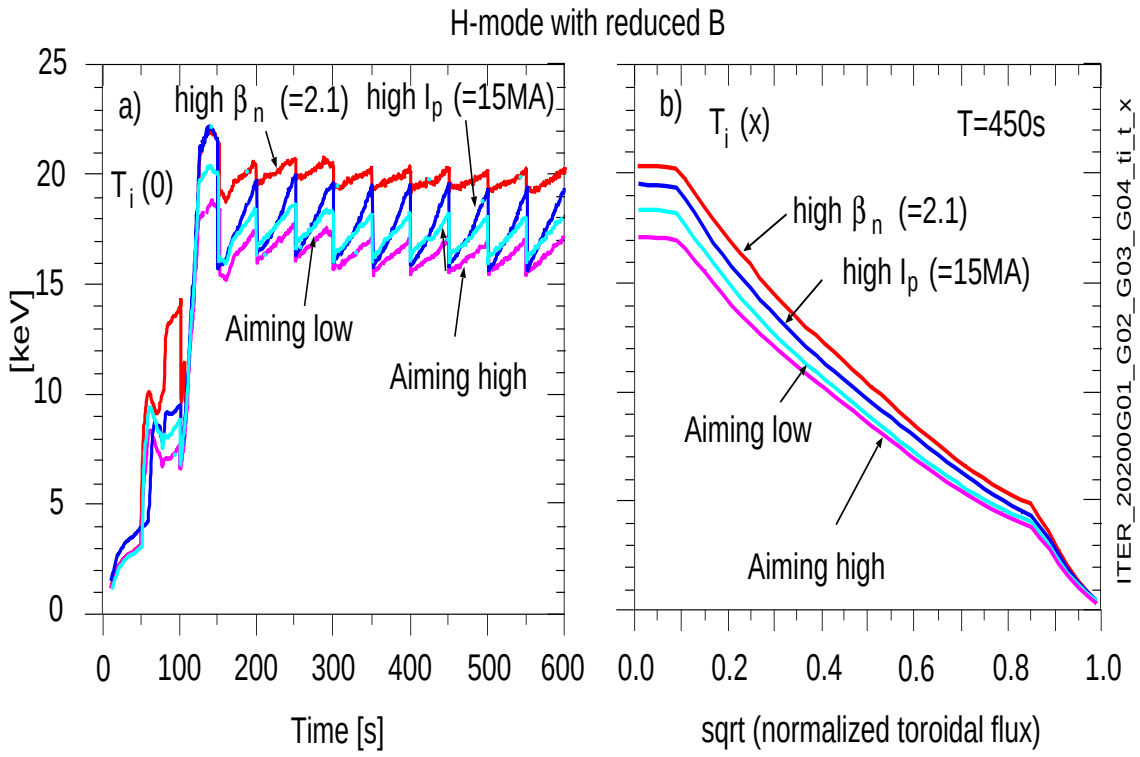
H-mode with reduced B
a)
high β n (=2.1)
high I p (=15MA)
T i (0)
[keV]
Aiming low
Aiming high
Time [s]
b)
T i (x)
T=450s
high β n (=2.1)
high I p (=15MA)
Aiming low
Aiming high
sqrt (normalized toroidal flux)
ITER_20200G01_G02_G03_G04_ti_t_x

Figure 24.

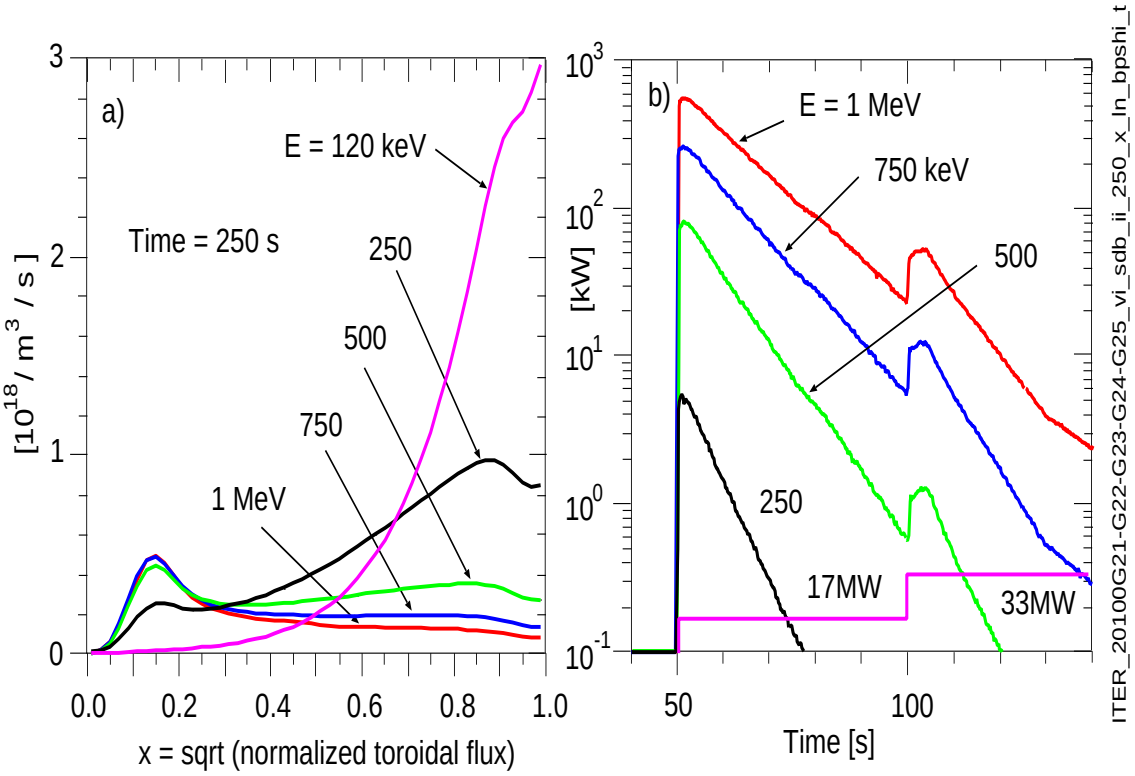
a)
E = 120 keV
Time = 250 s
250
500
750
1 MeV
[10^18 / m^3 / s]
x = sqrt (normalized toroidal flux)
b)
E = 1 MeV
750 keV
500
250
17MW
33MW
[kW]
Time [s]
ITER_20100G21-G22-G23-G24-G25_vi_sdb_ii_250_x_In_bpshi_t

Figure 25.

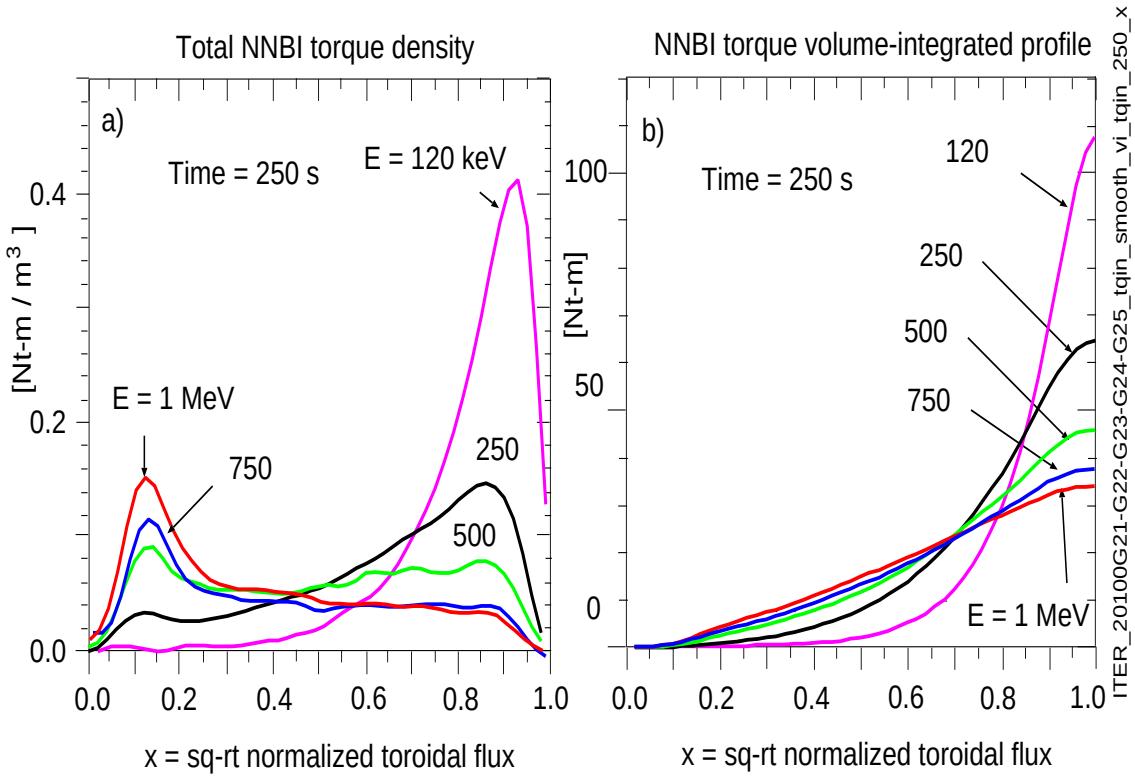

Figure 26.

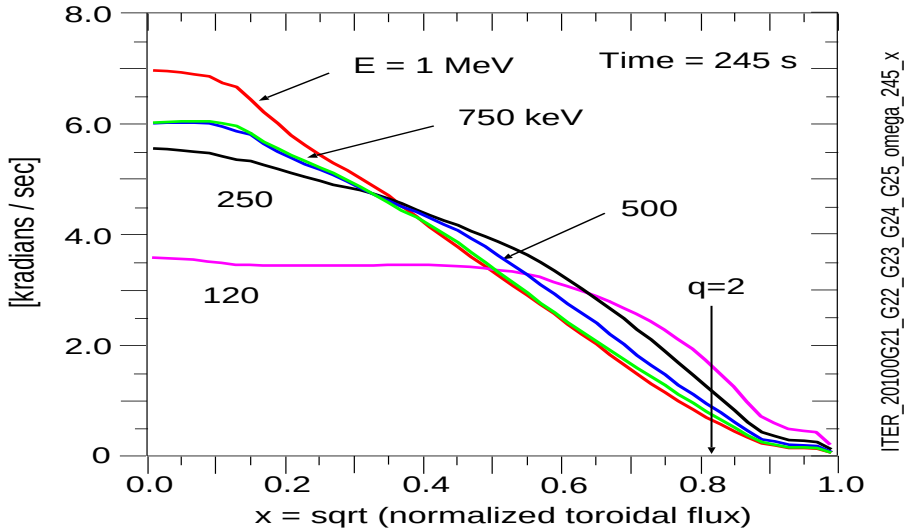

Figure 27.

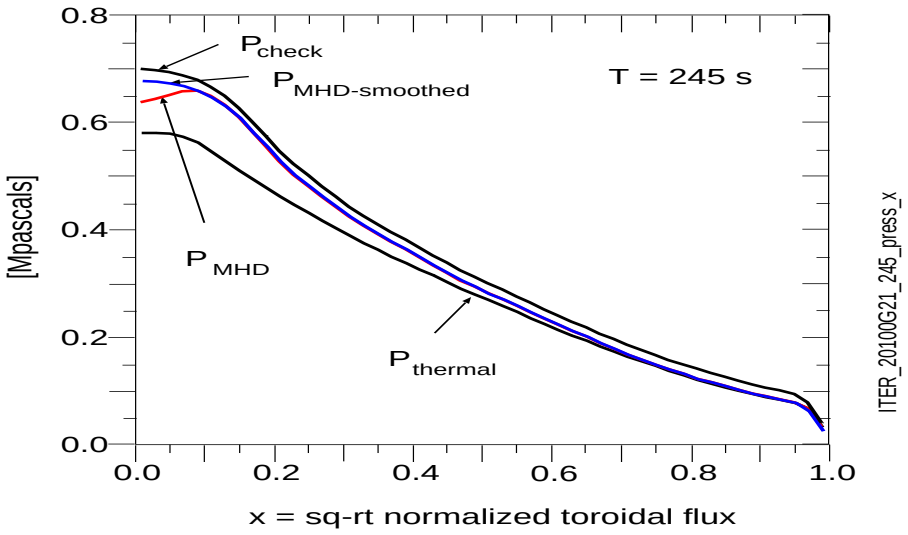
0.8
0.6
0.4
0.2
0.0
[Mpascals]
P check
P MHD-smoothed
T = 245 s
P MHD
P thermal
0.0
0.2
0.4
0.6
0.8
1.0
x = sq-rt normalized toroidal flux
ITER_20100G21_245_press_x

Figure 28.

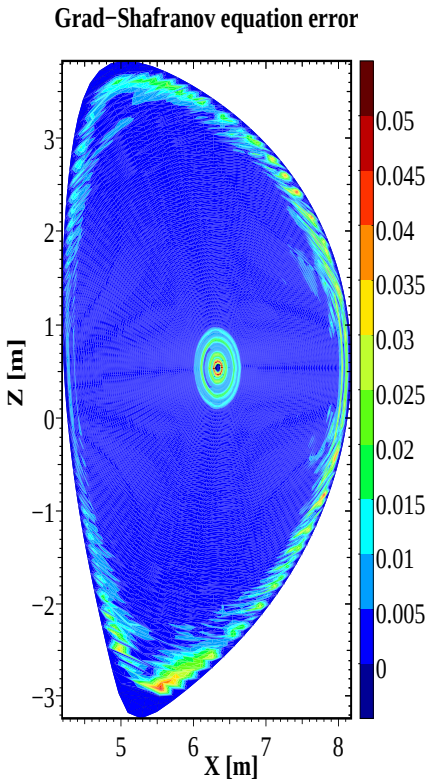
Grad−Shafranov equation error
Z [m]
X [m]
3
2
1
0
−1
−2
−3
5
6
7
8
0.05
0.045
0.04
0.035
0.03
0.025
0.02
0.015
0.01
0.005
0

Figure 29.

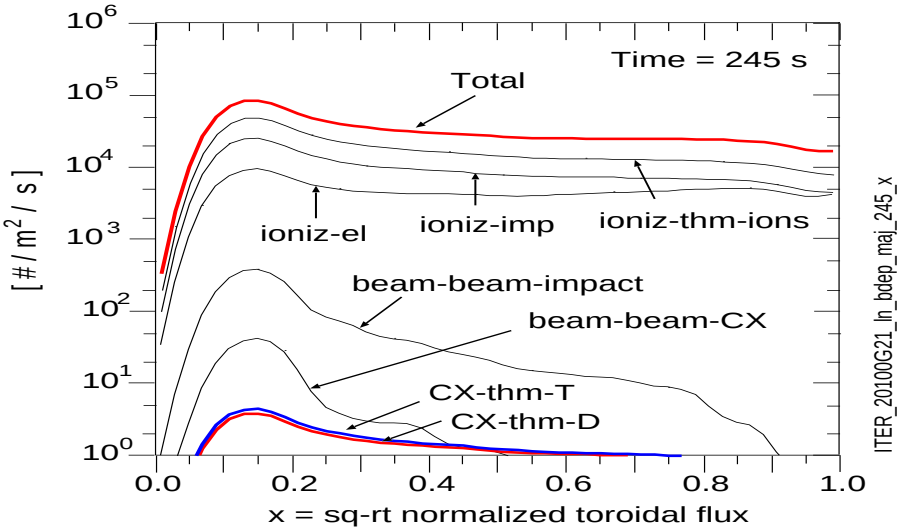

Figure 30.

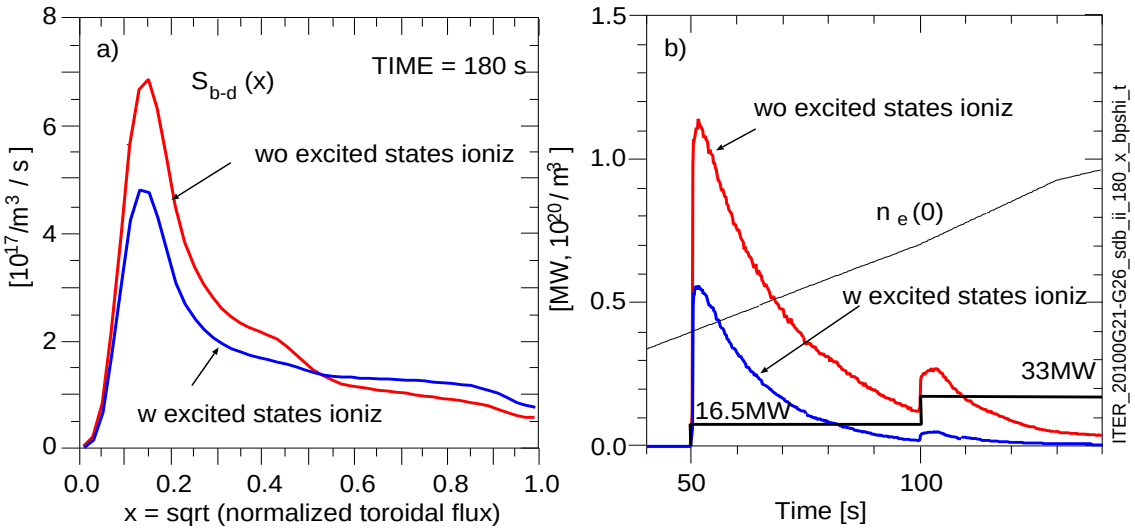

Figure 31.

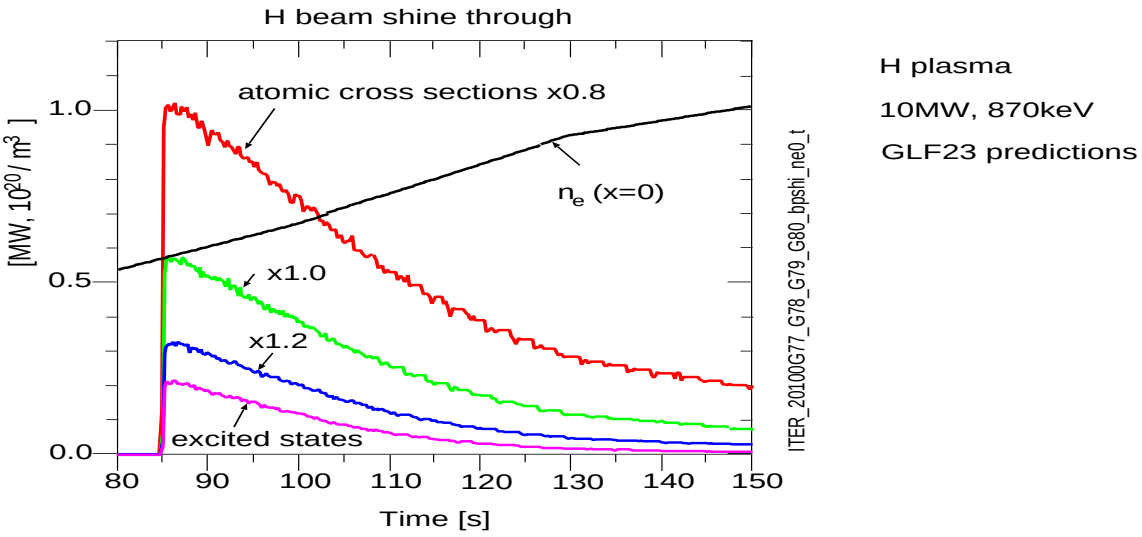

Figure 32.

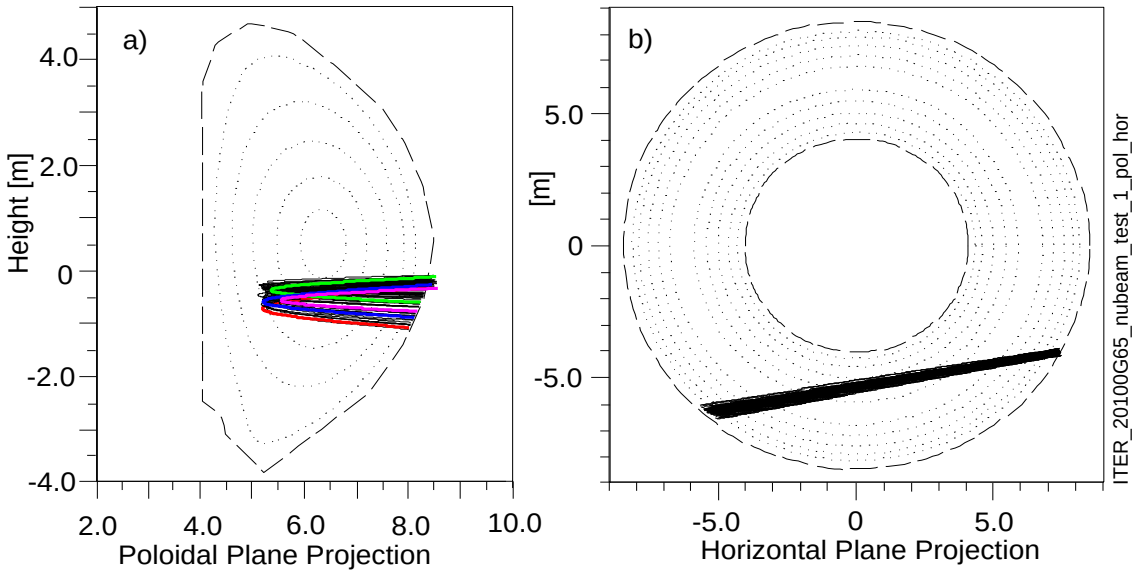

Figure 33.

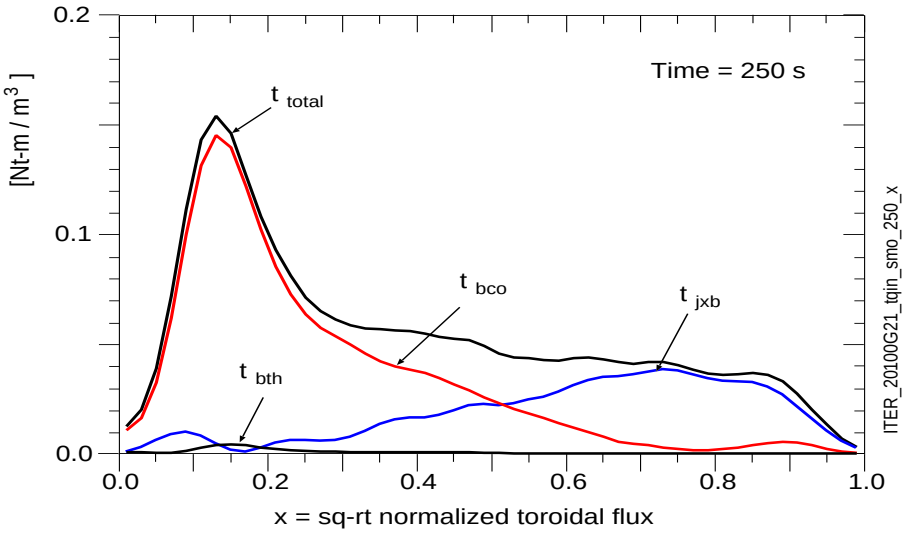
Time = 250 s
t total
t bco
t jxb
t bth
[Nt-m / m3]
x = sq-rt normalized toroidal flux
0.0
0.1
0.2
0.0
0.2
0.4
0.6
0.8
1.0
ITER_20100G21_tqin_smo_250_x

Figure 34.

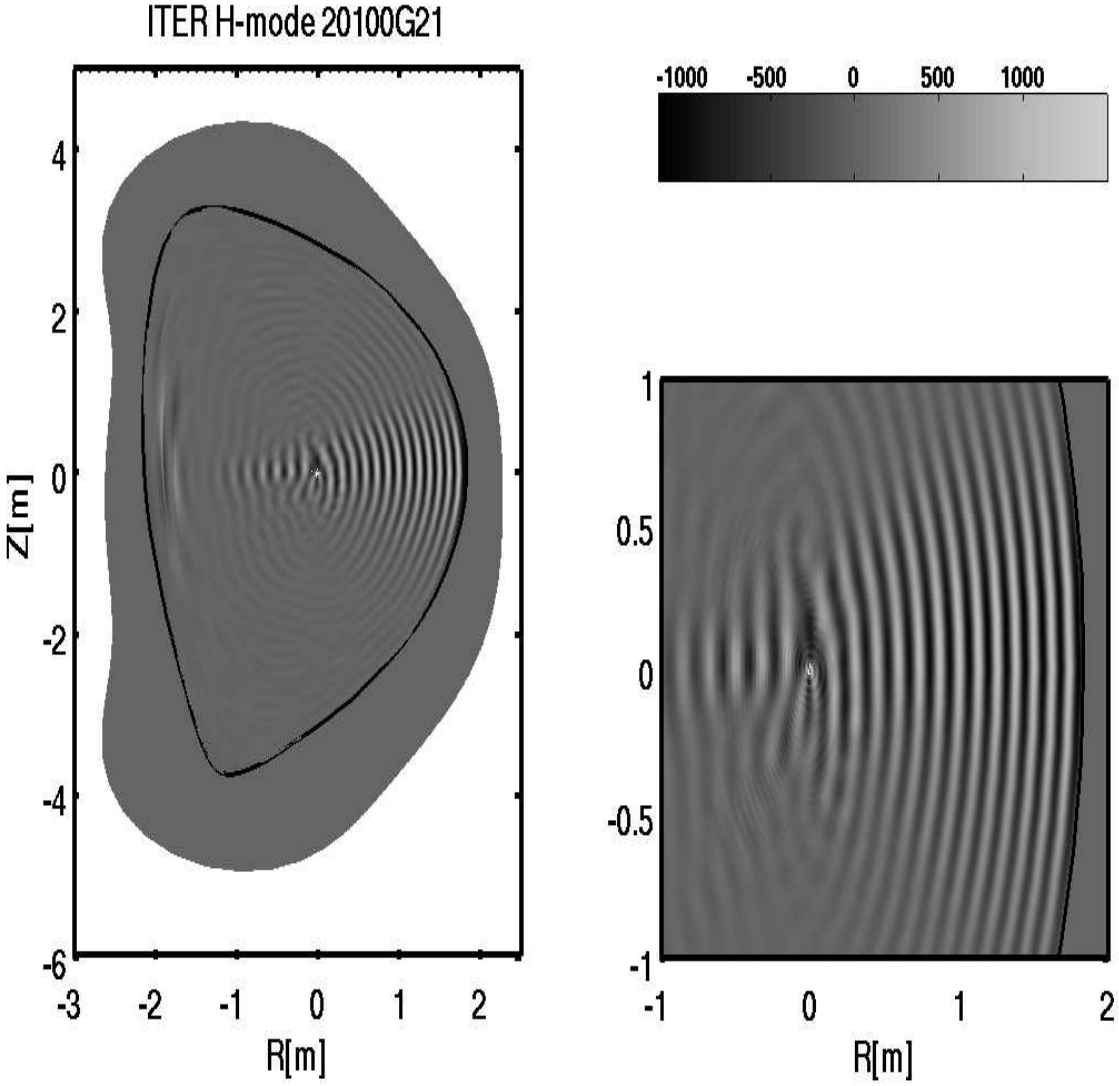

Figure 35.

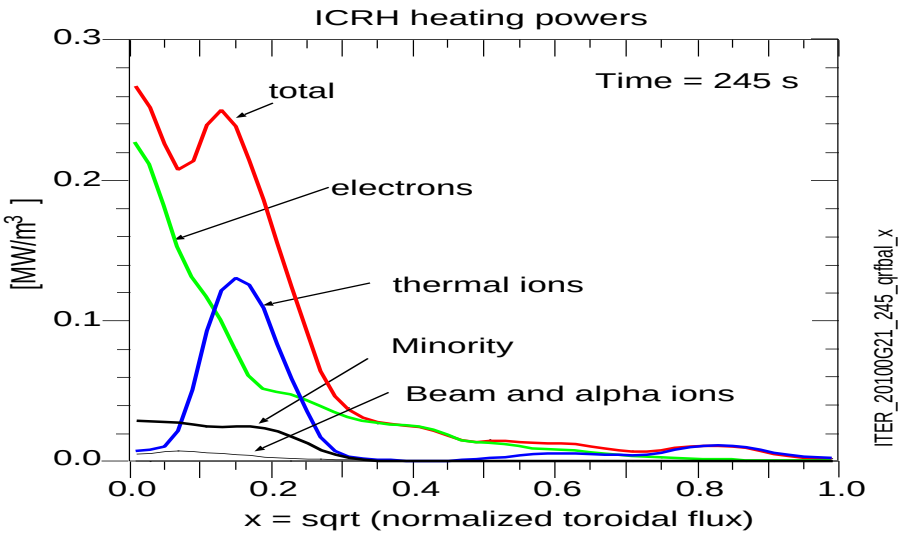
ICRH heating powers
Time = 245 s
total
electrons
thermal ions
Minority
Beam and alpha ions
[MW/m3]
x = sqrt (normalized toroidal flux)
0.0
0.1
0.2
0.3
0.4
0.6
0.8
1.0
ITER_20100G21_245_qrfbal_x

Figure 36.

The Princeton Plasma Physics Laboratory is operated
by Princeton University under contract
with the U.S. Department of Energy.

Information Services
Princeton Plasma Physics Laboratory
P.O. Box 451
Princeton, NJ 08543

Phone: 609-243-2750
Fax: 609-243-2751
e-mail: pppl_info@pppl.gov
Internet Address: http://www.pppl.gov